Innovative self-sensing fiber-reinforced cemented sand with hybrid CNT/GNP

IOP Publishing Smart Materials and Structures
Smart Mater. Struct. **30** (2021) 105034 (26pp) https://doi.org/10.1088/1361-665X/ac2108

Innovative self-sensing fiber-reinforced cemented sand with hybrid CNT/GNP

Mohammadmahdi Abedi[1], **Raul Fangueiro**[2,3,*] **and António Gomes Correia**[1]

[1] Department of Civil Engineering, ISISE, University of Minho, Campus de Azurém, 4800-058 Guimarães, Portugal
[2] Department of Mechanical Engineering, University of Minho, Campus de Azurém, 4800-058 Guimarães, Portugal
[3] Centre for Textile Science and Technology, School of Engineering, University of Minho, Guimarães, Portugal

E-mail: rfangueiro@dem.uminho.pt

Received 9 April 2021, revised 20 July 2021
Accepted for publication 25 August 2021
Published 13 September 2021

Abstract

This study is a systematic attempt to develop a self-sensing fiber-reinforced cemented sand (CS) with high physical, mechanical, durability, and piezoresistivity performances. In this route, different concentrations of Dyneema, glass, and polypropylene (PP) fibers were incorporated into CS containing 0.17% hybrid carbon nanotubes and graphene nanoplatelets. The specimens were fabricated using the standard Proctor compaction method and tested at the optimum water content. The mechanical, microstructural, and durability performances of the specimens were evaluated through various types of tests. Further, the piezoresistivity of the specimens was evaluated under compression cyclic loads using the four probes method. The incorporation of 1.0% glass and Dyneema fiber as the optimum percent increased the unconfined compression strength (UCS) (29% and 82%, respectively) and the maximum dry density of the CS; however, reinforcing of the specimens with PP fiber at a concentration in the range of 0.5%–1.5% generally reduced the UCS of the specimens. The pullout test results exhibited a considerable interfacial performance for the Dyneema fiber. The CS reinforced with 1.0% Dyneema and glass fiber demonstrated a lower weight loss after 12 wetting and drying cycles compared to other specimens. The maximum gauge factors were also achieved for Dyneema fiber-reinforced CS. The outcomes of this study, balanced with sustainable issues, contribute to the development of the new era of smart structures, with applications to roller-compacted-concrete dams, rammed earth, and particularly in structural layers in transportation infrastructure.

Keywords: self-sensing, piezoresistivity, fiber-reinforced, stabilized sand, sustainability

(Some figures may appear in colour only in the online journal)

1. Introduction

Currently, various structural health monitoring techniques, i.e. electric strain gauges, PZT-based piezoelectric sensors, fiber Bragg grating sensors, etc, have been introduced to detect the actual stress or strain state of infrastructures for applications in different fields, such as monitoring damage, transportation, and traffic flow [1–3]. Contrary to many advances, most of these available techniques involve a limited number of sensors distributed in a large area of the infrastructures. Furthermore, the low durability, heterogeneity, production complexity, and incompatibility of their detection mechanism with geomaterial mechanical behaviors have made many of these techniques incompetent [4–6].

Among all structural health monitoring methods, cement-based piezoresistive self-sensing composites have attracted more attention from researchers to overcome these limitations and achieve a real-time integrated system for infrastructure monitoring [7–9]. The main idea of a self-sensing

* Author to whom any correspondence should be addressed.

cementitious gecomposite is to monitor the stress/strain states in cementitious geomaterials based on a fractional change in the electrical resistance. This means that the cementitious geomaterials must be conductive [10].

For this purpose, different kinds of conductive fillers may be dispersed into the non-conductive cementitious composite [11–13]. The continuous conductive pathways generated by conductive fillers based on percolation and electron tunneling effects, have a considerable contribution to the transmission of electric current among the cementitious composite structure [14, 15]. These conducting paths are disturbed when the composites are subjected to stress, strain, damage, or deformation, which results in changing the electrical resistivity [16, 17]. The type of conductive phase is one of the effective factors in the sensitivity and performance of the cement-based self-sensing composites [10, 18, 19].

Although, the various types of conductive fillers, such as steel fibers, nickel powder, iron oxide nanoparticles, carbon black, and carbon fiber, have been used as a conductive phase in the cementitious matrix [20, 21], graphene nanoplatelets (GNPs), and carbon nanotubes (CNTs) have attracted more attention for developing piezoresistive self-sensing cementitious composite due to their unique electrical and mechanical properties [18, 22, 23].

Besides, recent studies have proven the potential of CNT/GNP synergic effects to create ultrasensitive affordable self-sensing cementitious composites [10, 23, 24]. The hybrid combination of these 1D and 2D carbon nanomaterials (CNMs) with high aspect ratios, can improve the percolation and electron tunneling mechanism, which leads to the reduction of the percolation threshold and consequently eliminates the concerns regarding the production costs as well as the porosity and agglomeration formation. The nanoscale conductive paths formed by these CNMs are also more sensitive against the small strain and stress compared to the microscale conductive paths created by micro fiber fillers [10, 25].

The incorporation of these CNMs into the cementitious composite also enhances the mechanical, microstructural, and durability performances by the bridging and/or deviation of cracks, increasing the cement hydration rate and their filler function mechanism [26–28]. However, the low ductility of the cementitious composites which is also intensified by CNTs in some cases [29, 30] still remains as one of the cement base's self-sensing weaknesses.

The brittle behavior of nano-intruded cementitious composite exacerbates their weakness against cracking. This is particularly important in cementitious stabilized sand (CS), which is one of the most widely used geomaterials in infrastructure construction. What's more, it should be noted that the more ductile composite behavior leads to a more appropriate piezoresistive response against the stress/strain and, consequently, the data scatter will be reduced. Based on the literature, fiber reinforcement is one of the common and widely used methods to improve the ductility behavior of CSs [31–33].

Fibers can radically moderate brittle behavior and enhance mechanical performance [34]. Glass and polypropylene (PP) fibers are two conventional available fibers utilized for CS reinforcement [35, 36]. Due to the low stiffness of PP fibers, they adapt well with the CS in terms of ductility. CS reinforced with the glass fiber (GF) with non-crystallizable components has attracted substantial attention in different applications predominantly owing to being fairly light, cost-effective, and enjoying rather fine relative mechanical properties, including flexural and tensile moduli as well as flexibility during processing and biodegradation. In addition, they have the least harm to the processing equipment and ample renewable resources [37–41].

In the last decade, a novel fiber with a high strength-to-weight ratio was developed, called Dyneema. Dyneema is an ultra-high-molecular-weight polyethylene (UHMWPE) that is stronger than steel and aramid fibers up to 15 and 1.4 times, respectively [42]. High strength and modulus, high durability and resistance against aggressive chemical agents, and low toxicity have made Dyneema attractive [42]. Hence, in this study, a CNT/GNP intruded CS was reinforced by these fibers to develop a self-sensing cementitious geocomposite with high ductility. Indeed, one of the main purposes of fiber inclusion into the CS is to decrease the stiffness with an increase in the maximum strain and to consequently prevent micro crack propagation as well as to produce long-term performance enhancement.

The outcomes of this study provide an extensive contribution to the new era of smart structures, in this case with applications to roller-compacted-concrete dams, rammed earth, ground improvement, and particularly in structural layers in transportation infrastructures, especially in critical zones, such as transition zones. This self-sensing composite material will have the capacity to detected material damages, anticipate maintenance needs, and avoid failures, which, in some structures, may cause fatalities.

In this route, and following the previous findings applied to a mortar [10, 24, 43], different concentrations of glass, PP, and Dyneema fibers were incorporated into the cylindrical specimens after surficial acid treatment, and the maximum dry density and optimum water content were evaluated. This approach in the manufacture of the specimens is different from previous studies, aiming for applications for the type of structures mentioned earlier. The mechanical properties of the specimens were investigated by unconfined compressive strength (UCS) tests after 28 d of hydration as well as by the tangent modulus at 50% of the maximum strength. These properties are important in the characterization and design of several geotechnical structures [44–47]. Additionally, the microstructural performance of reinforced CS was investigated using various tests. The interfacial properties of the fibers and matrix were evaluated by mechanical and chemical analysis. The durability of the specimens against wetting and drying cycles was also evaluated (long term performance). Furthermore, the piezoresistivity behaviors of reinforced CS were investigated under cyclic compression loading by the four probes method to evaluate the self-sensing capacity of the novel materials.

2. Materials and methods

2.1. Raw materials

To fabricate CS, CEN Standard sand, with siliceous and clean particles was used. This sand is classified as well-graded sand following the Unified Soil Classification System. The particle size distribution curve and physical properties of the sand are presented in figure 1 and table 1. The grading, measured by sieving, complies with the EN 196-1 and of ISO 679:2009 standard requirements. In this study, ordinary Portland cement type I (CEM I 42.5R) was also utilized as a binder in order to stabilize the sand. The grain size curve and mineralogical compositions of cement are presented in figure 1 and table 2.

A multi-wall CNT (MWCNT) and multi-layer type GNP were utilized as conductive fillers in this study. The specifications of the MWCNTs and GNPs are summarized in table 3 [24]. The morphology of hybrid GNPs/CNTs in a dry mix state was also investigated using a scanning electron microscope (SEM), and this is depicted in figure 2. The x-ray diffraction (XRD) patterns of CNTs and GNPs are shown in figure 3.

In order to hybrid the CNT/GNP dispersion, Pluronic F-127 was used as a noncovalent surfactant. This surfactant is a nonionic triblock copolymer surfactant composed of a central hydrophobic chain of polyoxypropylene and two hydrophilic chains of polyoxyethylene placed on two sides. The molecular structure of Pluronic F-127 is similar to polycarboxylate, which is typically used as a cementitious composites superplasticizer [48].

Hence, this surfactant was found to be compatible with cementitious composites and could possibly enhance its dry density owing to the improved consistency of CS. In addition, tributyl phosphate (TBP, 97%) with $^1/_2$ of the surfactant weight ratio was used as an antifoam to prevent porosity formation caused by surfactant function following the previous research [49]. The TBP and PF-127 molecular structures are depicted in figure 4 [24]. Since the average optimum length of fiber used for cementitious composite reinforcement is around 10–14 mm [50–52]; in this study, alkali-resistant glass fibers (AR-GF), split film type of polypropylene (PP), and Dyneema fibers with an average length of 12 mm were used for CS reinforcement. The physical properties of the fibers are listed in table 4.

In this study, sulfuric acid 97% and hydrofluoric acid 40% were used for surface treatment of the fibers.

2.2. Dispersion method of CNT/GNP

The presence of strong surface van der Waals forces between CNMs due to their high specific surface area leads to their high tendency to agglomeration. Hence, the effective transfer of CNT/GNP supreme properties to the composite is strongly dependent on their dispersion status. Besides, the dispersion method should be attentively chosen to prevent adverse effects on the cement hydration process and/or inherent properties of nanomaterials [53, 54]. Following the above discussion, a feasible and compatible dispersion method that was developed recently was used in this study [24]. In this route,

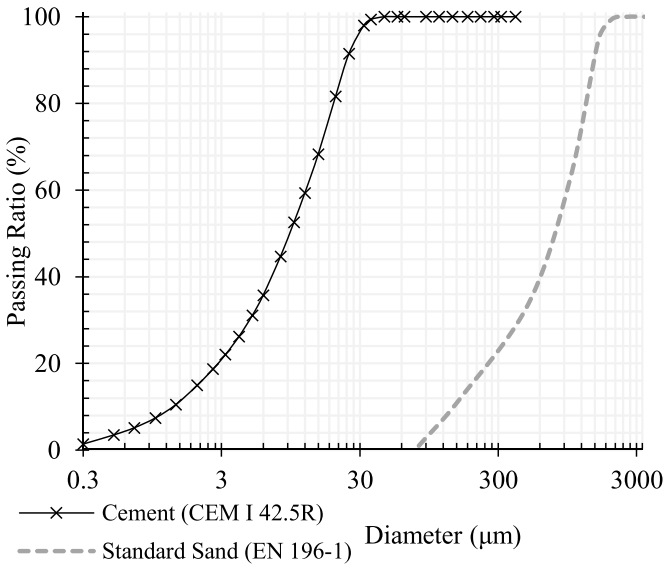

Figure 1. The particle size distribution (PSD) curve of the sand and cement [10, 43].

Table 1. Physical properties of the sand [10].

Mesh size (mm)	0.08	0.16	0.5	1	1.6	2
Cumulative retained (%)	99 ± 1	87 ± 5	67 ± 5	33 ± 5	7 ± 5	0
Specific gravity G_s	2.67		Cu	7.5	Cc	1.8

TBP was first dissolved into the required optimum water content of fiber-reinforced CS over 12 h with a magnetic stirrer at 800 rpm min^{-1}. It should be noted that the required optimum water content (ω_{opt}) concentration for each case of fiber-reinforced CS was measured by the compaction standard test, and, for this purpose, dry CNT/GNP was dispersed among the dry materials using the mechanical mixer and with gradual water concentration increases. After completely dissolving the TBP, 10% of Pluronic F-127 (by weight of CNMs) was added to the suspension and mixed for 1 more hour using the magnetic stirrer mixer at the same speed.

Based on the literature, the optimum hybrid CNT/GNP concentration that was obtained for the development of a self-sensing cementitious composite was around 0.17% (1:1, by weight of the sand) by considering the physical behavior [10, 43]. Hence, in this study, the same concentration was used. The hybrid CNT/GNP was added to the suspension and stirred continuously for 1 more hour, and the suspensions were then placed in a sonicator bath with 80 W output power and, 45 kHz frequency for 3 h. In addition, a digital temperature regulator composed of the circulation system, sensors, and a radiator was used to adjust the temperature during the ultrasonication at 40°C. Under these specific mixing conditions, negligible structural damage was expected for the CNMs.

Raman spectroscopy (figure 5) was also performed on CNMs using laser excitation with a wavelength of 532 nm in order to ensure about the absence of adverse effects on the nanomaterials structural quality, such as edge-type defects,

Table 2. Chemical composition and properties of the cement [43].

SiO_2 (%)	Al_2O_3 (%)	Fe_2O_3 (%)	MgO (%)	CaO (%)	Na_2O (%)	TiO_2 (%)	K_2O (%)	MnO (%)	P_2O_5 (%)	SO_3 (%)	LOI[a] (%)	Fineness ($m^2\ kg^{-1}$)	Specific gravity ($kg\ dm^{-3}$)	Initial setting time (min)[b]	Soundness (mm) [b]	Blaine's surface ($cm^2\ g^{-1}$)[b]
19.9	4.7	3.38	1.3	63.93	0.17	0.245	0.446	0.079	0.063	2.54	2.97	360	3.15	194	1.1	4220

[a] (Loss on ignition) EN 196–2.
[b] EN 196–3.

Table 3. Multi-wall carbon nanotube (MWCNT) and graphene nanoplatelets (GNP) specifications [24].

GNP										
Surface area (m^2 g^{-1})	Density (g cm^{-3})	Carbon content (%)	Tensile modulus (GPa)	pH value (30 °C)	Tensile strength (GPa)	Layers	Dimension		Form	Part number
120–150	0.6	>99.5	1000	7–7.65	5	<20	Thickness 4–20 nm	Diameter 5–10 μm	Gray powder	TGN201
MWCNT										
Surface area (m^2 g^{-1})	Density (g cm^{-3})	Color	Outside diameter (nm)	Length (μm)	Ash (wt%)		Carbon content (%)		Part number	
350	0.27	Black	<8	30–10	<1.5		>98		GCM327	

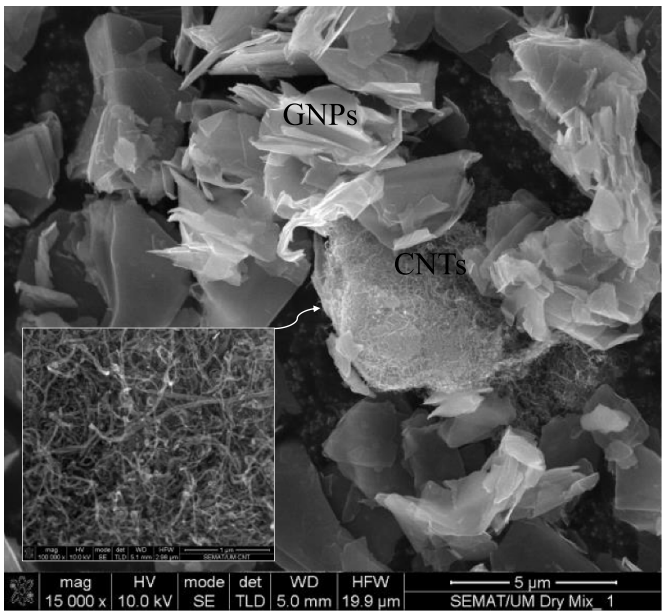

Figure 2. GNP and CNT morphology (dry mix).

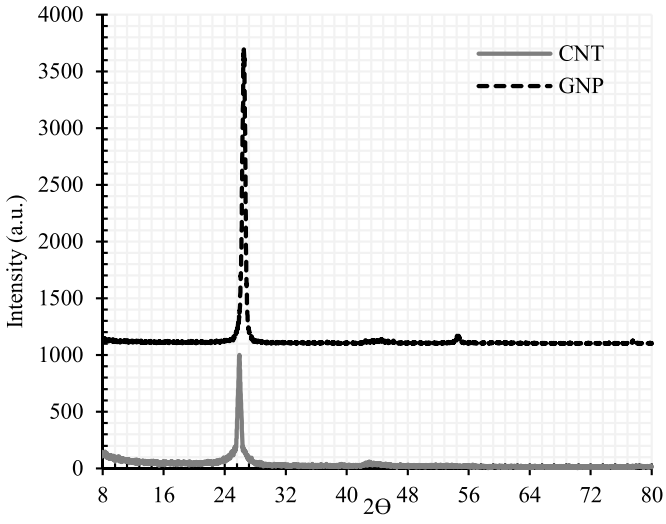

Figure 3. X-ray diffraction (XRD) patterns of CNT and GNP.

reduction of the aspect ratio, and sp2 domain crystallinity (La), which cause a deleterious influence on the mechanical and electrical performances [24, 55, 56].

2.3. Surface treatment of the fibers

The surfaces of the fibers were treated using the chemical method to increase the interaction and adhesion between the cementitious matrix and fibers [57–61]. In this route, The PP and Dyneema fibers were submerged into a bath of sulfuric acid and sodium dichromate solution for 24 h at 50 °C, and the glass fibers were dipped into hydrofluoric acid 40% for 18 h at 40 °C. Thereafter, the fibers were washed with water and dried at room temperature. This treatment might cause asperity on the fiber surface, and likely causes a chemical reaction between the fibers and the cement matrix.

2.4. CS specimens fabrication

In the case of sand, the required cement concentration for soil improvement usually varies by around 10% owing to the target strength of the enhanced soil [62–64]. In this study, 10% of the cement (by weight of the dry sand) was utilized for CS fabrication, and all of the fiber-reinforced specimens were fabricated at the optimum water content (ω_{opt}) of the Standard Proctor test.

In this route, the mixing sequence adopted was as follows: the cement and sand were poured into the Hobart mixer and then blended with the stainless steel blade's rotational speed at 140 m min^{-1} for 1.5 min. Then, a nanomaterial suspension prepared by ω_{opt} (for each fiber concentration) was sprayed into the mixture and blended at a 285 m min^{-1} higher speed for another 2.5 min. Thereafter, surficial treated fibers were added to the mixture and stirred for a further 1.5 min by the same rotational speed. The concentration of the fibers used in this study were 0.5%, 1.0%, and 1.5% by weight of the dry sand. The mixture was then poured into a plastic bag to prevent moisture loss.

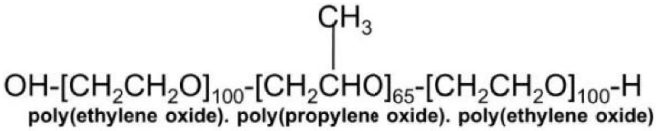

(a)

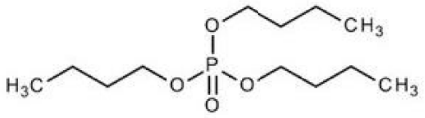

(b)

Figure 4. Chemical structures of: (a) Pluronic F-127 and (b) Tributyl phosphate 97% [24].

Table 4. Physical properties of glass, polypropylene, and Dyneema fibers.

Alkali-resistant (AR)-glass fiber (GF)						
Tensile strength (GPa)	Linear mass density of fibers (g km^{-1})	Density (kg m^{-3})	Elastic modulus (GPa)	Elongation at break (%)	Length (mm)	Diameter (μm)
3.2	9600	2700	73.1	4.4	12	31
Ultra-high-molecular-weight polyethylene (UHMWPE) (Dyneema)						
Tensile strength (GPa)	Linear mass density of fibers (dtex)	Elastic modulus (GPa)		Elongation at break (%)	Length (mm)	Diameter (μm)
3	440	10.3		5.6	12	14.5
Polypropylene (split film)						
Tensile strength (MPa)	Density (kg m^{-3})	Elastic modulus (GPa)		Elongation at break (%)	Length (mm)	Section dimension (μm)
54	910	4.31		15	12	36 $\times$ 640

The fiber-reinforced CS cylindrical specimens were fabricated by the compaction method according to the standard compaction following ASTM D698. Split molds with dimensions of 101.6 $\times$ 116.4 mm were filled with the wet mixture in three equal-height layers. A calculated amount of the well-mixed wet mixture was measured (to an accuracy of 0.01 g), shed into the split molds, and then compacted carefully by a metal tamper to the desired height (controlled by a caliper to an accuracy of 0.02 mm).

After compaction, the surfaces of the specimens were carefully leveled and sealed. The specimens were extracted after 24 h and cured under the water for 28 d. As shown in figure 6, four copper mesh (as electrodes) were also embedded into specimens used for piezoresistivity experiments.

The mixture moisture also was measured after compaction to ensure minimal water evaporation. The specimen's identification was conducted based on the variation of fiber types and concentration as listed in table 5.

In other to investigate the interfacial properties of the fibers and cement matrix, single-fiber pullout tests were used. Due to the small size and fragility of the fibers, a special method was used following the literature [65, 66]. For the preparation of the specimen, special plastic molds were used which showed in figure 7(a).

The thickness of the initial cured samples is too wide and hence, the single fiber would break during the test. Following Li [67], the theoretical length of fiber was calculated around 6 mm for the successful pullout of the fiber without rupture, which indicates that the specimen's thickness, i.e. the fiber embedded length in the matrix, would not exceed 6 mm. In fact, to successfully obtain the entire force-displacement curve during pulling out, the real CF embedded length should be

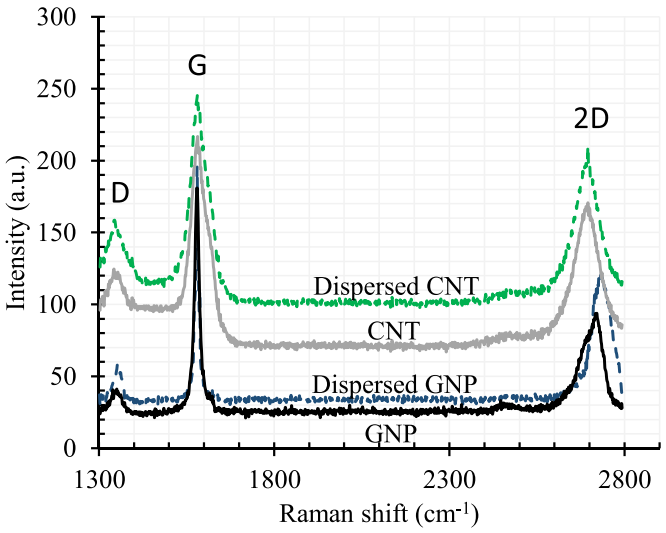

Figure 5. Raman spectroscopy of CNTs and GNPs after dispersion.

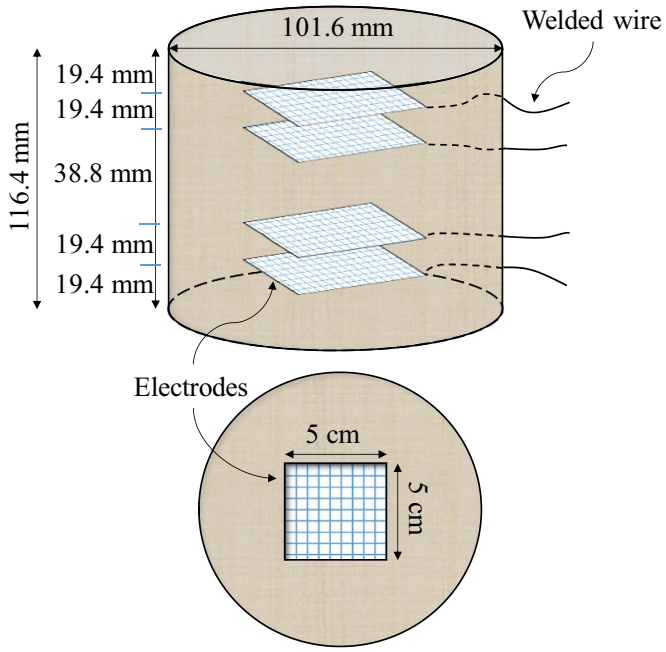

Figure 6. Representation of the specimen geometry and electrode layout.

Table 5. Mix proportions of the reinforced cemented sand (CS), carbon nanomaterial (CNM), polypropylene (PP).

Sample ID[a]	CNM (%)[b]	Glass fiber (%)	PP fiber (%)	Dyneema fiber (%)	Cement (%)
Plain CG	0.17	—	—	—	10
CGG (0.5%)	0.17	0.5	—	—	10
CGG (1.0%)	0.17	1	—	—	10
CGG (1.5%)	0.17	1.5	—	—	10
CGP (0.5%)	0.17	—	0.5	—	10
CGP (1.0%)	0.17	—	1	—	10
CGP (1.5%)	0.17	—	1.5	—	10
CGD (0.5%)	0.17	—	—	0.5	10
CGD (1.0%)	0.17	—	—	1	10
CGD (1.5%)	0.17	—	—	1.5	10

[a] All of the concentration are by weight of the dry sand.
[b] By equal proportion (1:1).

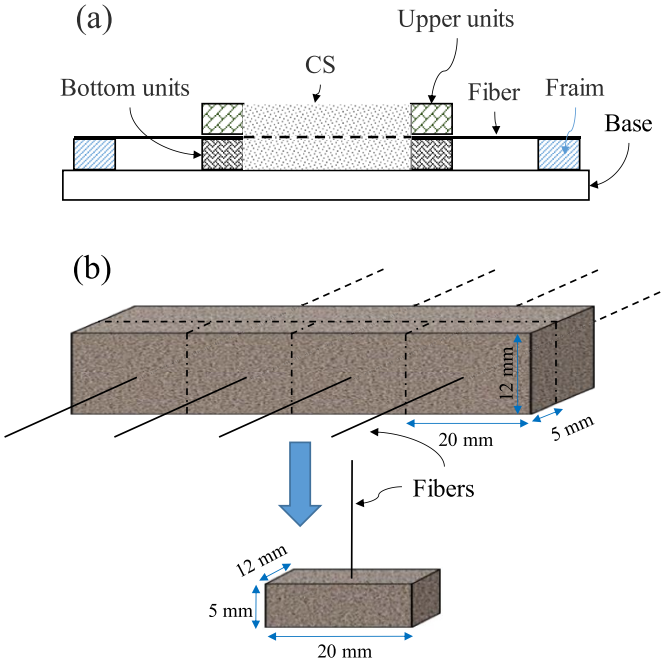

Figure 7. The process of pull-out specimen fabrication: (a) cross-section of the mold and (b) dimensions of the specimen.

further limited. Hence, after 28 d of curing, specimens were cut to dimensions of 20 mm × 12 mm × 5.0 mm as shown in figure 7(b).

2.5. Mechanical, microstructural, and durability evaluations

For the mechanical evaluation of fiber-reinforced CS, we used the UCS tests following the ASTM/D2166M standard. The results were calculated by the mean of at least three specimens. As the modulus of elasticity for cementitious geomaterials is typically expressed by the modulus at 50% of the peak stress [44, 68, 69], the Tangent $E_{(50\%)}$ of fiber-reinforced composites by different fiber types and concentrations was calculated at 50% of the maximum compression stress.

In order to evaluate different fiber concentrations on the maximum dry density and ω opt of fiber-reinforced CS, standard compaction tests were carried out following the ASTM D697-78 standard. Besides, the specimen fracture surfaces were investigated using SEM through the secondary electrons mode and an acceleration voltage of 10 kV after coating with an Au–Pd thin film (30 nm) in a high-resolution sputter coater (Cressington 208HR). The energy-dispersive x-ray spectroscopy (EDX) analysis was performed at 3 kV using an energy-dispersive x-ray spectrometer coupled with the SEM.

Fourier transform infrared spectroscopy (FTIR) and EDX were performed to analyze the surface structure of the treated fibers. For this purpose, the fibers were purified by washing and precipitation with deionized water and then dried for 10 h

at 50 °C in a vacuum dry container. An ultrasonic nondestructive test was conducted for microstructural investigation following the BS EN 12504-4 standard through two probes along the longitudinal axis of the specimens. The weight loss of the fiber-reinforced CS was measured in terms of a composite durability investigation after 12 cycles of wetting and drying according to ASTM D 559-96.

The single fiber pullout tests were conducted at a rate of 0.02 mm s^{-1}, by a universal testing machine. The test results are an average of at least five specimens and three bonding parameters including bond strength (τ_{max}), frictional bond strength (τ_{fr}), and chemical debonding energy (G_d) were calculated by equations (1)–(3) as follow [70, 71]:

$$\tau_{max} = \frac{P_{max}}{\pi d_f l_e}, \tag{1}$$

$$\tau_{fr} = \frac{P_{fr}}{\pi d_f l_e}, \tag{2}$$

$$G_d = \frac{2(P_{max} - P_{fr})^2}{\pi^2 d_f^3 E_f}, \tag{3}$$

where P_{fr} is frictional pullout load, P_{max} is maximum pullout load, l_e is fibers embedded length, d_f is fibers diameter, and E_f is fibers elasticity modulus. In the case of PP fibers, the cross section was assumed to be circular with a diameter of 7 μm. This assumption has no quantitative effect on the circumference of the fiber.

2.6. Piezoresistivity behavior investigations

For the piezoresistivity investigation of the fiber-reinforced CS, the cylindrical specimens with embedded electrodes were dried first at 70 °C for 72 h after 28 d of hydration to eliminate the effects of moisture on electrical conductivity. In this study, the four probes technique (figure 6) was used for the evaluation of fractional changes in the electrical resistivity (FCR) of reinforced CS subjected to cyclic axial compression loading. In this route, a 100 Ω reference resistor was connected to the outer probes in a series powered by a direct current (DC) source (20 V).

The power supply was conducted for 45 min to stabilize the supply in the fiber-reinforced specimens. The variation of voltage between the two inner probes and resistor were measured by a digital multimeter. As illustrated in figure 8, three cycles of 5 KN axial compression loading with a rate of 50 N s^{-1} were used for the CS piezoresistivity behavior evaluation.

The voltage variations of the fiber-reinforced CS were obtained from an average of three measurements. The resistivity $\rho(t)$ of the specimens was calculated by combining the first and second Ohm's law equations (equations (4) and (5) respectively) as presented in equation (6) [72]:

$$R(t) = \frac{V_1(t)}{I(t)} = \frac{V_1(t)}{V_2(t)/100} \tag{4}$$

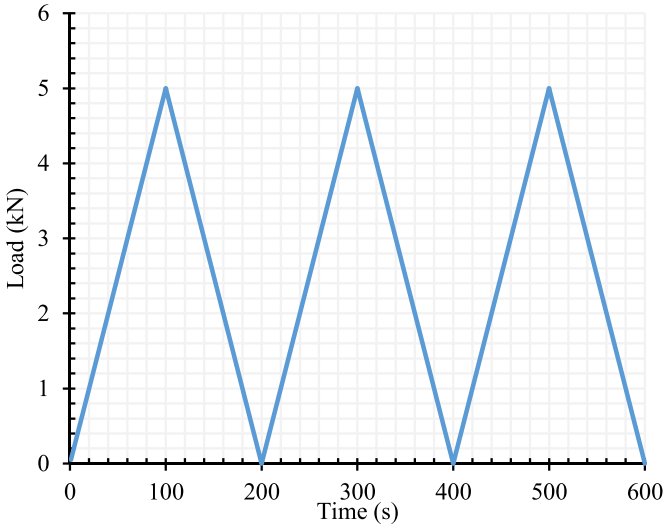

Figure 8. Cyclic compression loading pattern.

$$R(t) = \rho(t)\frac{L}{A} \tag{5}$$

$$\rho(t) = \frac{V_1(t)}{V_2(t)/100} \times \frac{A}{L}, \tag{6}$$

where $V_1(t)$ and $V_2(t)$ are the inner probes and resistor voltage, respectively; $I(t)$ is the current between the outer electrodes; $R(t)$ is the resistance between the two inner probes; A is the contact surface between the electrode and specimen; and L is the spacing between the inner electrodes. The FCR was calculated using equation (7) for the following assessment of CS piezoresistivity:

$$FCR = \frac{\rho(t) - \rho_0}{\rho_0}, \tag{7}$$

where ρ_0 is the initial electrical resistivity, which is measured before loading, and $\rho(t)$ is the resistivity at time (t) during the test. In order to evaluate the sensitivity of fiber-reinforced CS against the strain, the gauge factor (GF) is also defined as the relative change in electrical resistivity over the strain (equation (8)):

$$GF = \frac{FCR}{\varepsilon} \tag{8}$$

where ε is the applied strain along the force axis.

3. Results and analysis

3.1. Fiber surficial characterizations

The FTIR spectra of the pure and treated fibers are illustrated in figure 9. The results confirmed the presence of different functional groups on the surface of the fibers caused by the sulfuric acid treatment of the PP and Dyneema fibers and hydrofluoric acid treatment of the glass fibers.

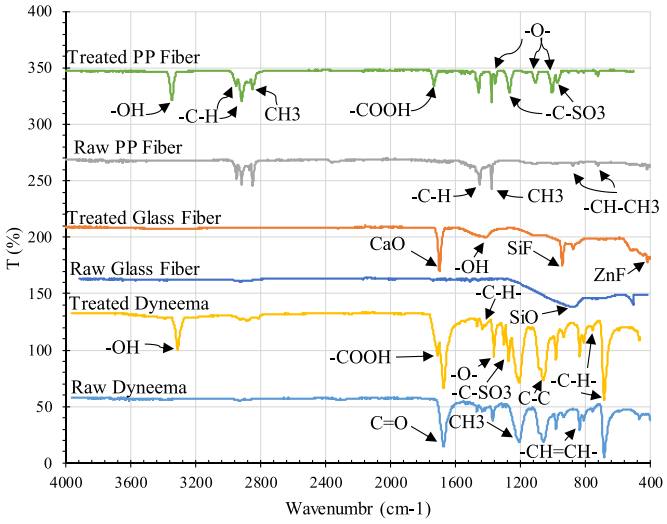

Figure 9. Fourier transform infrared spectroscopy (FTIR) spectra of raw and treated fibers.

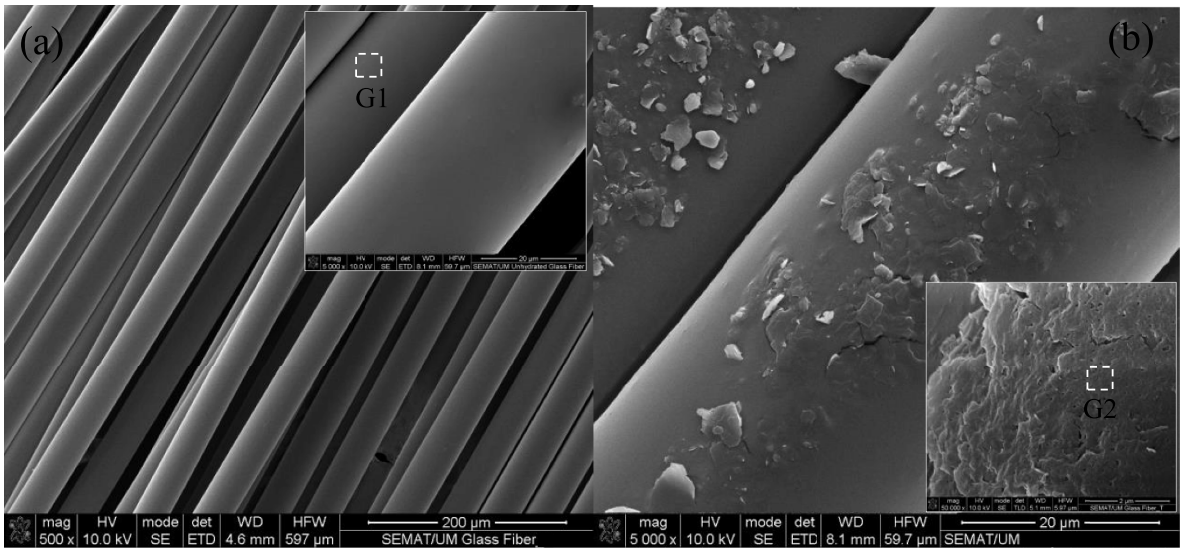

Figure 10. Surface morphology of glass fibers: (a) pure glass fiber and (b) hydrofluoric acid treated glass fiber. (The marked areas in the scanning electron microscopy (SEM) images are the areas selected for energy-dispersive x-ray spectroscopy (EDX) analysis.)

As can be observed, the treated PP and Dyneema fibers had the oxygen groups of –O–, –OH, –C–SO_3^-, and –COO^-- supported by new peaks at 1360, 1102, 1025 cm^{-1} (–O–), 3350 cm^{-1} (–OH), 1360, 1264, 985 cm^{-1} (–C–SO_3^-), and 1730 cm^{-1} (–COOH). However, the number of functional groups seems to be higher at the surface of Dyneema fibers. The FTIR analysis of the pure PP and Dyneema fibers showed the characteristic peaks at 1375 cm^{-1}, from the symmetric bending vibration of CH_3; at 1450 cm^{-1}, from the symmetric stretching vibration of –C–H in CH_3, at 1166, 972, 840, and 808 cm^{-1}, from the vibration rocking of –CH_2 and CH_3, and the stretching of CH–CH_3 and CH–CH_2. Hydrofluoric acid treated glass fiber also demonstrated some functional groups, including –OH, CaO, SiF, and ZnF supported by 1419 cm^{-1} (–OH), 1700 cm^{-1} (CaO), 1031 cm^{-1} (SiF), and 417 cm^{-1} (ZnF). The morphology of the fiber surfaces was also investigated with SEM, which is shown in figures 10–12.

As can be seen, the chemical reaction between fibers and acids during the treatment process, led to some irregularity and roughness on the surface of the fibers. These surface defects can cause a slight reduction in the tensile strength of the fibers, increasing the interaction and bonding between CS and fibers that can improve the anchor mechanism of the fibers and, consequently, increase the mechanical performance of the composite [73].

The chemical analysis results of the fiber surface are also listed in table 6.

The results showed that the chemical composition of the pure PP and Dyneema fibers almost included carbon, nitrogen, and oxygen elements. However, the EDX analysis results illustrated the presence of sulfur (S) and an increase in the amounts of oxygen after treatment by sulfuric acid. In the treated glass fibers, the existence of the fluorine element and increase of oxygen was clear due to the chemical

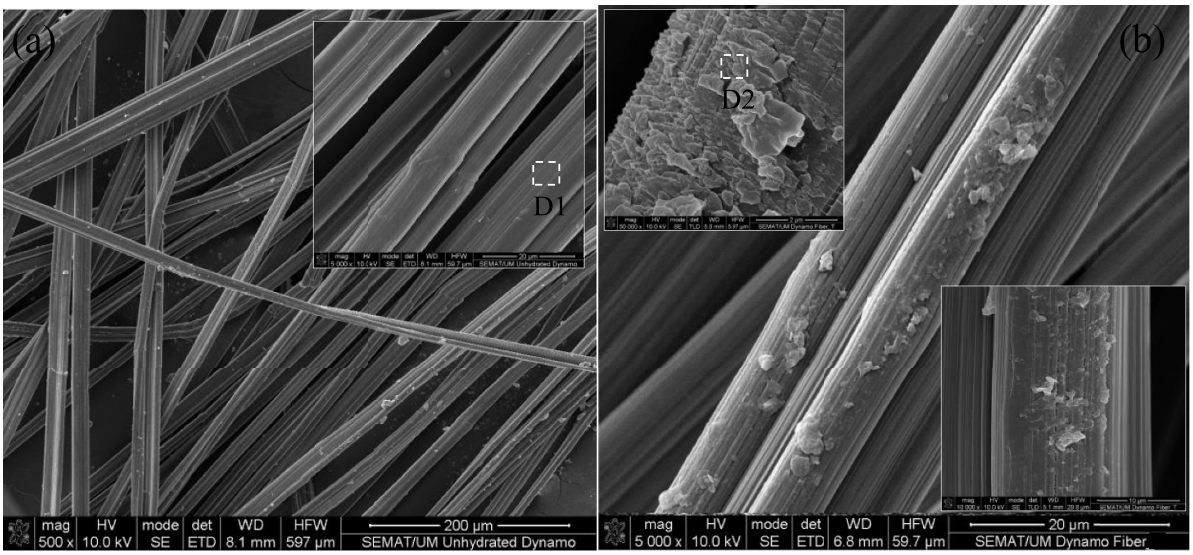

Figure 11. Surficial morphology of Dyneema fiber: (a) pure Dyneema fiber, (b) sulfuric acid treated Dyneema fiber. (The marked areas in the SEM images are the areas selected for EDX analysis.)

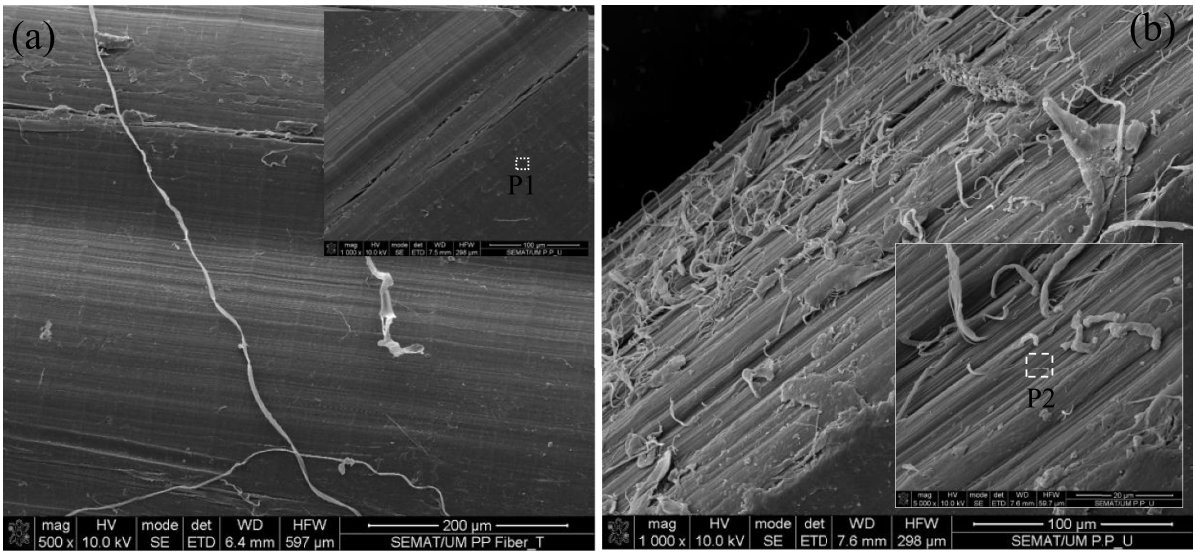

Figure 12. Surficial morphology of PP fiber: (a) pure PP fiber, (b) sulfuric acid treated PP fiber. (The marked areas in the SEM images are the areas selected for EDX analysis.)

Table 6. Chemical analysis of pure and treated fibers.

	Elements (%)										
Position	C	O	N	Ca	Al	Si	S	Mg	F	Zn	Zr
Figure 10 (G1)	20.3	13.72	—	18.1	5.62	24.1	—	1.17	—	4.1	12.9
Figure 10 (G2)	15.8	29.6		12.7	2.14	19.8	—	1.1	7.4	3.3	8.2
Figure 11 (D1)	78.09	5.6	16.3	—	—	—	—	—	—	—	—
Figure 11 (D2)	61.7	16.2	9.1				12.9				
Figure 12 (P1)	78.75	3.95	17.3	—	—	—	—	—	—	—	—
Figure 12 (P2)	64.8	14.7	11.9				8.6				

reaction of glass with hydrofluoric acid during the treatment process.

3.2. Compaction and microstructural investigations

The compaction curves of plain CS containing 0.17% CNMs and fiber-reinforced CS with different types and concentrations of the fibers are presented in figure 13.

The results showed that the incorporation of a certain amount of fiber concentration into the CS caused an increase of the maximum dry density. Indeed, an excessive increase in the fiber content reduced the dry density. The filler function of the fibers is heavily dependent on their geometry shapes and aspect ratio and the ductility of the fibers as subjected to the compaction energy. A schematic representation of the fibers filler mechanism is illustrated in figure 14.

As can be observed in figure 14(b), the rectangular cross-section of the PP fibers makes it difficult to embed them into the free spaces between this type of sand grains. Further, by increasing the PP fiber concentration, the gaps between the sand and cement particles were increased, which led to an increase in the optimum water content in the form of free water.

In the case of the glass and Dyneema fibers (figures 14(c) and (d)), however, the circular cross-section of the fiber with smaller dimensions improved the maximum dry density of the composite, and excessive increasing of fiber concentration caused an increment in porosity content and consequently reduced the maximum dry density of the CS.

In order to better evaluate the relation between fiber types, and concentration with the maximum dry density and optimum water content are illustrated in figure 15. As can be observed, the optimum concentration of glass and Dyneema fibers were obtained around 1.0%. However, the maximum dry density of Dyneema reinforced CS at the optimum concentration was more than with the glass fibers due to the higher aspect ratio of Dyneema fibers. Besides, as presented in figure 14, the incorporation of the PP fibers into the CS composite by a concentration in in range of 0.5%–1.5%, generally reduced the maximum dry density and increased the optimum water content.

The results of the saturation degree, which are shown in figure 16, also show the efficiency of Dyneema and glass fiber-reinforced CS in terms of the compressibility. The results showed that the saturation degree of the composite was generally reduced by the addition of the PP fibers, due to an increase in amounts of the void ratio.

In the case of glass and Dyneema fiber-reinforced composites, increasing the fiber concentration to 1.0% increased the saturation degree by reducing the void ration, while increasing the fiber concentration beyond 1.0% caused a decreasing trend in terms of the saturation status. These very interesting findings can be alternatively represented by $\gamma_d/\gamma_{d(\max)}$ vs. 'Sr–$(Sr)_{opt}$' as illustrated in figure 17. This unique relation agrees with the recent studies [74] that demonstrated that these laboratory results can be applied directly in the field. This is a major issue to support the use of these novel materials in practice.

The results of the ultrasonic nondestructive test for reinforced CS by different fiber types and concentration after 28 d

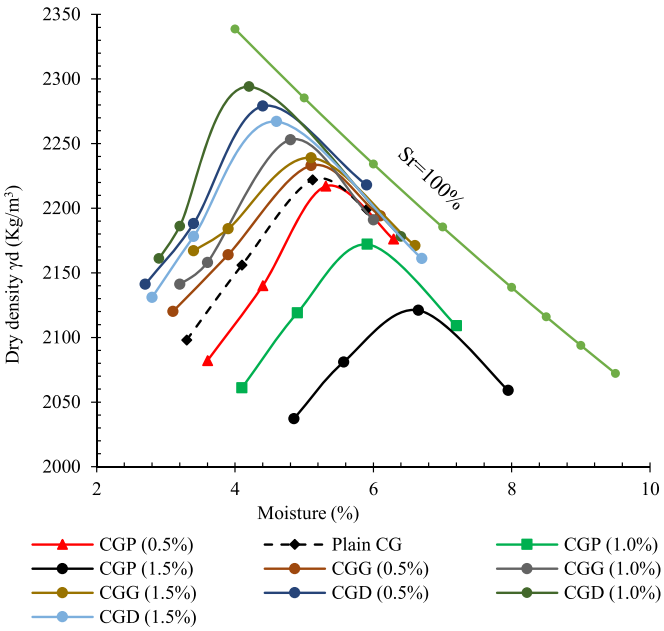

Figure 13. Compaction curves of reinforced CS with different types and concentrations of the fibers.

of the hydration period are shown in figure 18. The time of ultrasonic wave passing through the composite depended on the microstructure and density of the specimens. As can be observed the ultrasonic passing time was decreased for specimen CGP 0.5%, which contained 0.5% PP fiber. This indicates that the density of the specimen was increased after 28 d of cement hydration due to the growth of hydration products into the porosities and around the fibers that led to the embedding of them.

It should be noted that the excessive increase in the PP fiber concentration increased the ultrasonic wave passing time that was evidence of a density reduction.

A similar trend was observed for glass and Dyneema fibers, except that the optimum percentage of these types of fibers were obtained around 1.0%. The above outcomes are in line with the results of the mechanical investigations. Although the micro crack bridging and/or deviation mechanism of the fibers (figure 19) is the key factor in CS mechanical improvement, the filler function of the fiber was also not ineffective.

By incorporating a certain amount of the fiber into the CS, this fills the pores and spaces between the sand particles. The fibers buried among the hydration products during the cement hydration process can reinforce and bridge those products. When the plain CS is subjected to the load, usually in the early stages of loading, microscale cracks form inside the composite microstructure due to the brittle behavior of cementitious composites. While the optimum fiber-reinforced CS shows more resistance to cracking in the initial loading phase. When increasing the loads, nano-scale cracks grow into larger cracks at the micro-scale.

In the case of the proper bonding of fibers and the matrix, as long as the tensile force along the fiber length does not exceed the interaction force between the fibers or its pullout strength,

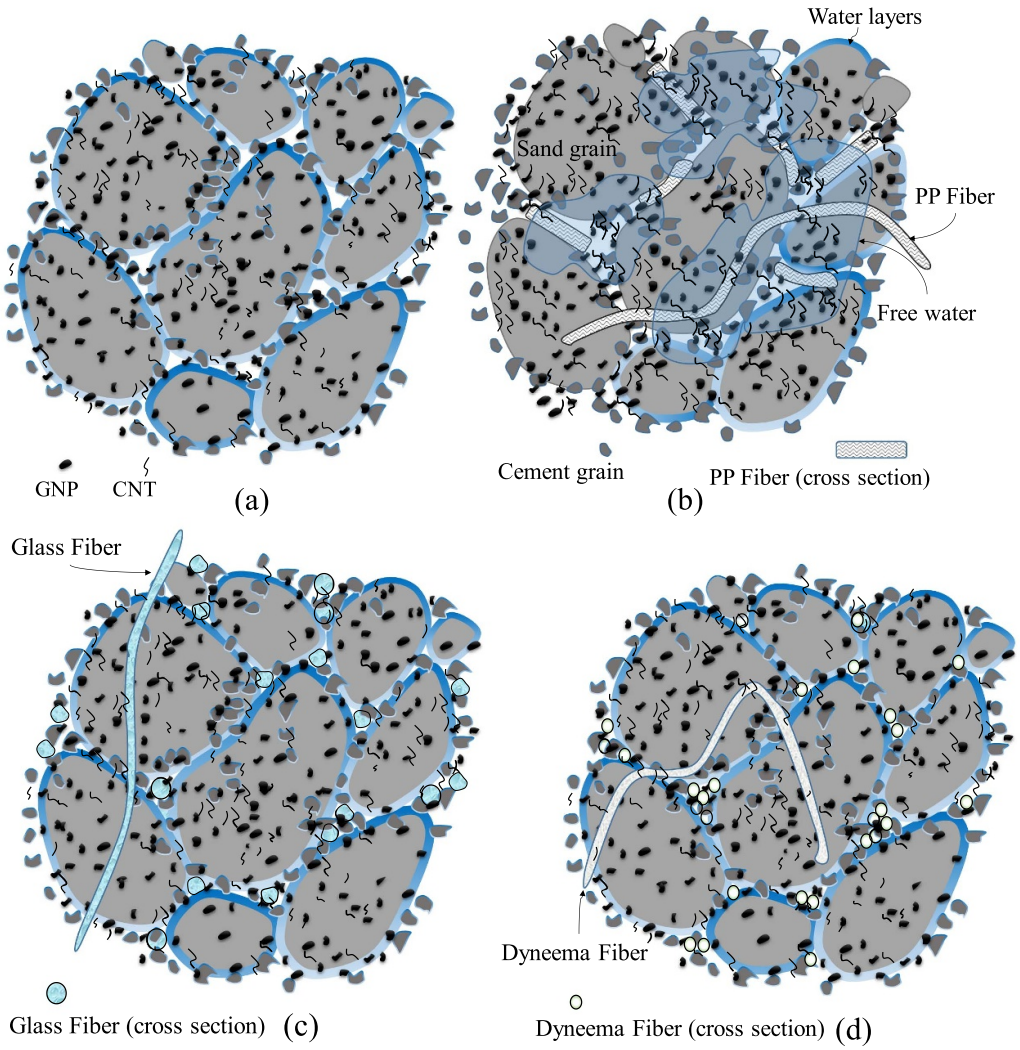

Figure 14. A schema of different fiber filler functions in CS: (a) without fiber, (b) reinforced with PP fibers, (c) reinforced with glass fibers, (d) reinforced with Dyneema fibers.

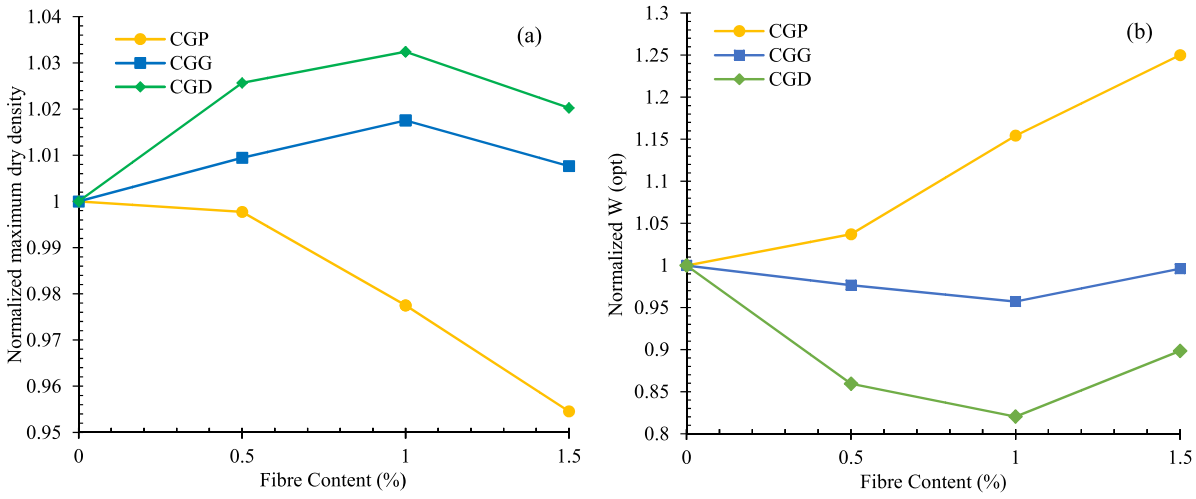

Figure 15. The relation between fiber types and concentration by the: (a) maximum dry density, (b) optimum water content.

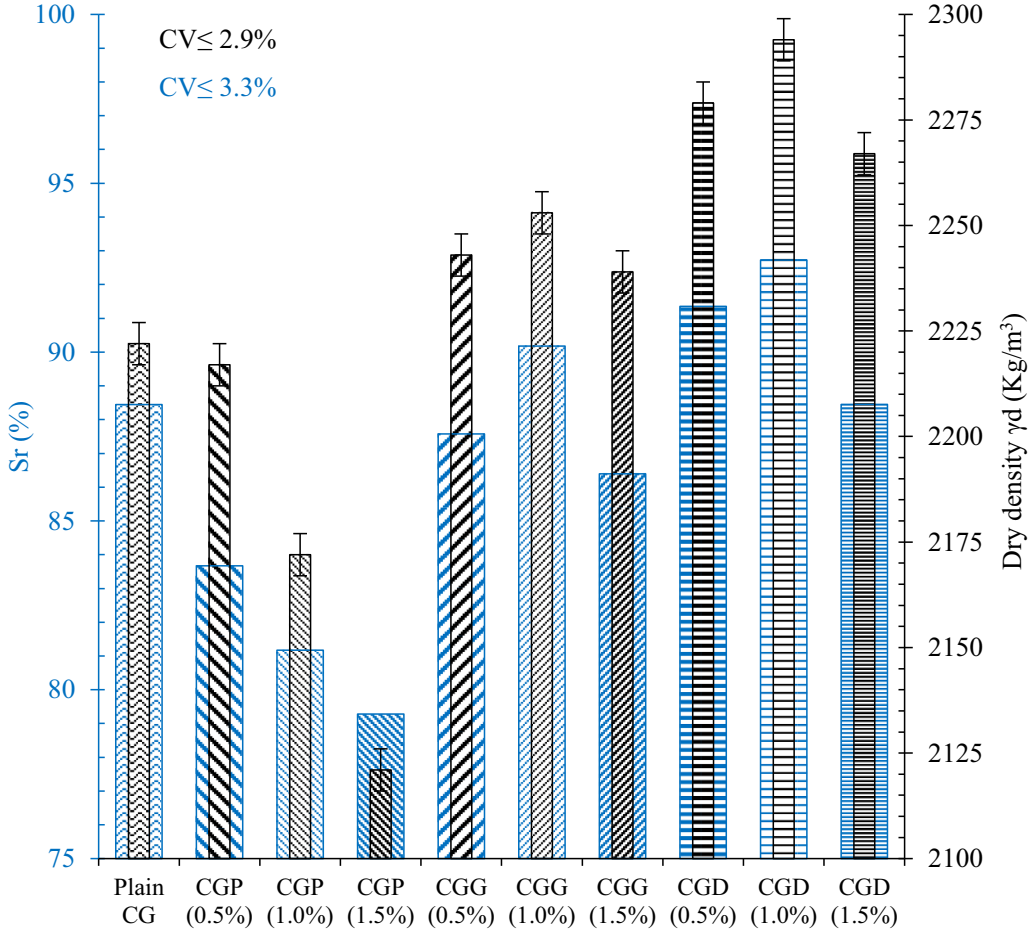

Figure 16. The saturation degree of reinforced CS with different fiber types and concentrations.

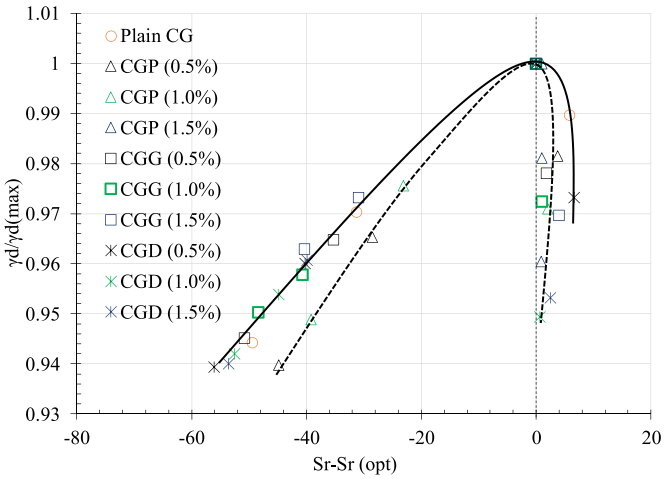

Figure 17. $\gamma_d/\gamma_d(max)$ vs. 'Sr–Sr (opt)' relations.

the specimen withstands the increasing load, and its ductility will also be increased.

The proper interaction between Dyneema and glass fiber surfaces with the cement matrix, which can be seen in figure 19, led to a halt in the crack expansion process by bridging and also deviation of the path. In next step, by the excessive increase of the load, two mechanisms are likely to occur, fiber extruding and fiber rupture (figure 20).

In the case of low interaction between the fiber surface and/or expansion of cracks in the region around the fibers and low shear strength of the matrix near them, the fibers are extruded from the cementitious composite.

As can be observed in figure 20, the low interaction between the PP fiber and cement matrix led to the fiber extruding, while the proper interaction between glass and Dyneema fibers led to glass fiber rupture and elongation in the Dyneema fibers due to withstanding the tension.

The dimensional and geometrical shape of the fiber cross-section, roughness, and status of the fiber surface in terms of rippling and porous texture are some of the crucial factors to enhance the fiber adhesion with a composite. Besides the existence of effective chemical functional groups can increase the fiber surface chemical bonding with the cementitious matrix.

The morphology of the Dyneema, glass, and PP fiber extracted from cementitious composite are illustrated in figures 21 and 22. As can be seen, the oxygen functional groups caused by acid treatment, which are discussed in section 3.1, made an approximately strong bond with the cement hydration products. On the surface of glass fiber, the oxygen and fluorine functional groups, made the surface ideal

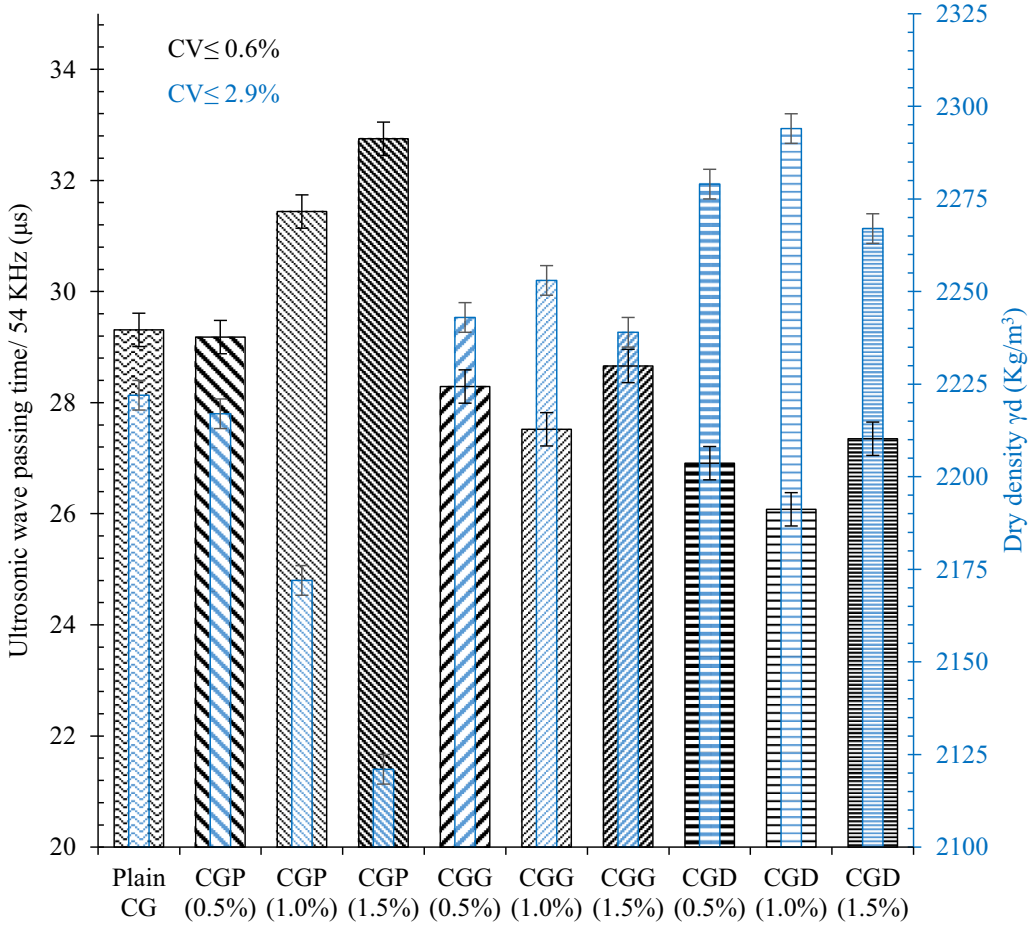

Figure 18. Ultrasonic wave passing times vs. the maximum dry density for reinforced CS by different fiber types and concentrations after 28 d of hydration.

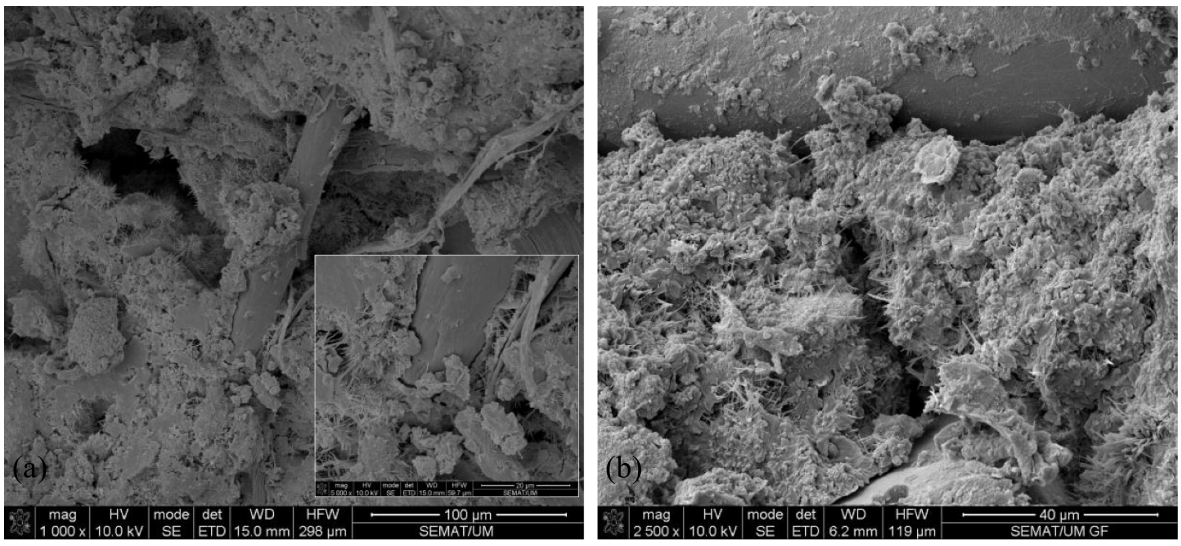

Figure 19. The mechanism of crack bridging and deviation: (a) Dyneema fiber, (b) glass fiber.

for growing hydration products. In the case of PP fibers, despite the presence of some oxygen functional groups caused by acid treatment, no proper bonding was observed between the surface and the cement matrix and only the surface roughness statute provided the required interaction with the composite. The reason for this might be attributed to the lower number of oxygen groups and their lower ability to bond with hydration products. In fact, the number of free electrons determines the

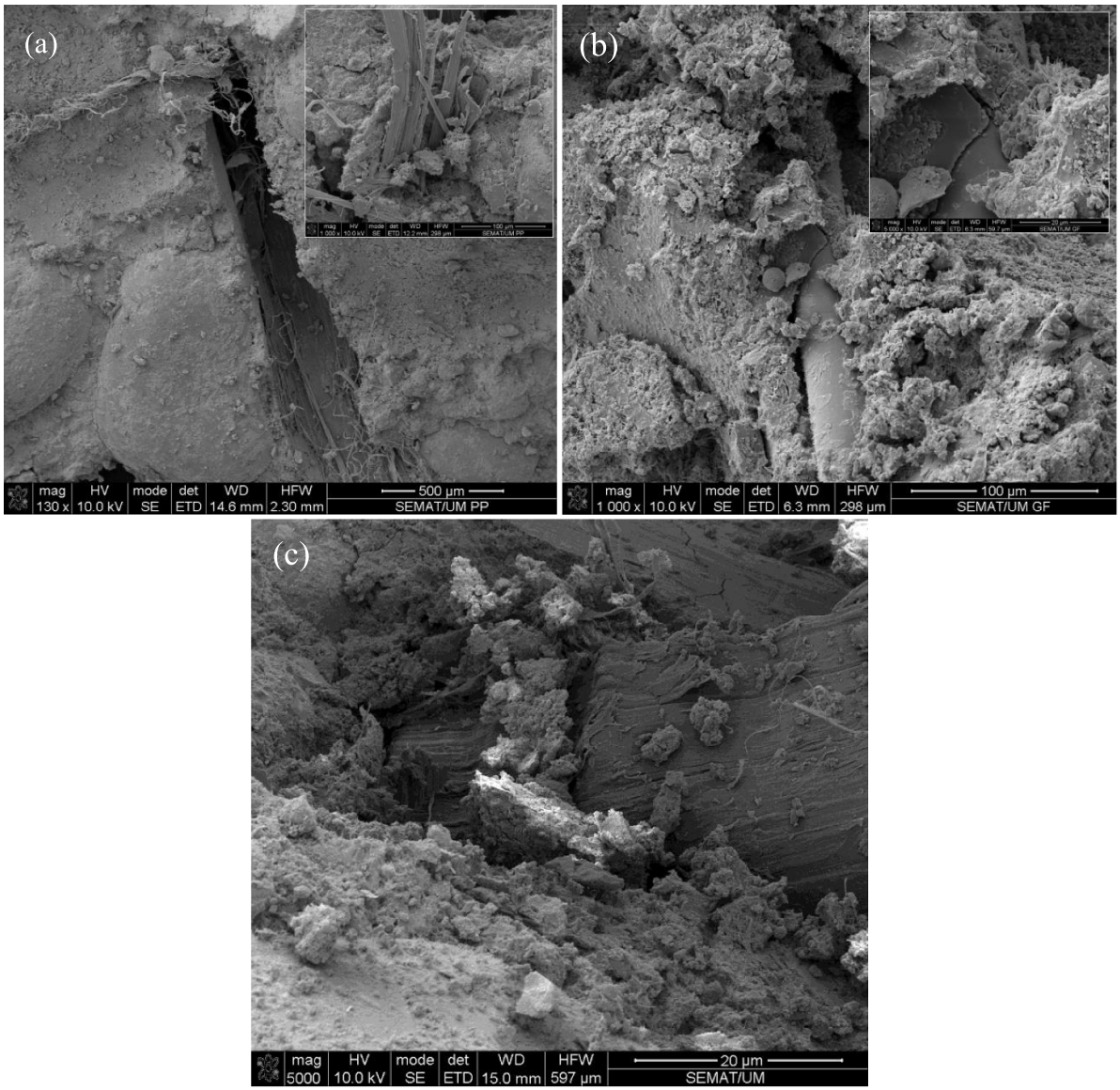

Figure 20. Morphology of the CS reinforced by fibers: (a) PP fiber (fiber extruding), (b) glass fiber (fiber rupture), (c) Dyneema fiber (fiber elongation).

ability of groups to bond, which depends on the structure and chemical reaction of the fibers during the treatment process [75].

The XRD patterns of treated and extracted fibers from the CS, as illustrated in figure 23, clarified new aspects of this issue. In Dyneema fibers, the chemical reaction between cement particles and oxygen functional groups led to the formation of calcium hydroxide (CH) on the surface of the fibers while in PP fibers, ettringite (AFt) crystals were formed on the surface. The dense structure of calcium hydroxide was more resistant vs. the brittle needle-shaped crystals of ettringite, which can be the reason for the proper bonding and interaction of Dyneema fibers with the cement matrix.

In order to, more accurate investigations on the interfacial performance of the fibers-matrix, the single fiber pullout tests were performed and interfacial properties such as bond strength (τ_{max}), frictional bond strength (τ_{fr}), and chemical debonding energy (G_d) were measured. The results of the typical successful pullout tests are presented in figure 24. Three main regions were observed at the pullout load slip curve in figure 24(a). Initially, a stable debonding process of the fibers happens along with the interface of fiber and matrix at the first region. In this zone, the embedded end of the fibers does not move. Meanwhile, the debonded length of the fiber increases until reaches the embedded length, and the fiber's pullout resistance grows up to P_{max}.

The measured displacements at this phase attributed only to the debonded fiber elastic stretching and the free length of the fibers. In the second region, the load suddenly declines from P_{max} to P_{fr} which is corresponds to the breaking of the chemical bond between the fiber and the matrix. Finally, at the third zone, at the slippage region, the load of the fibers is resisted by frictional forces [70, 76, 77]. Three bonding factors were calculated based on this behavior and results are

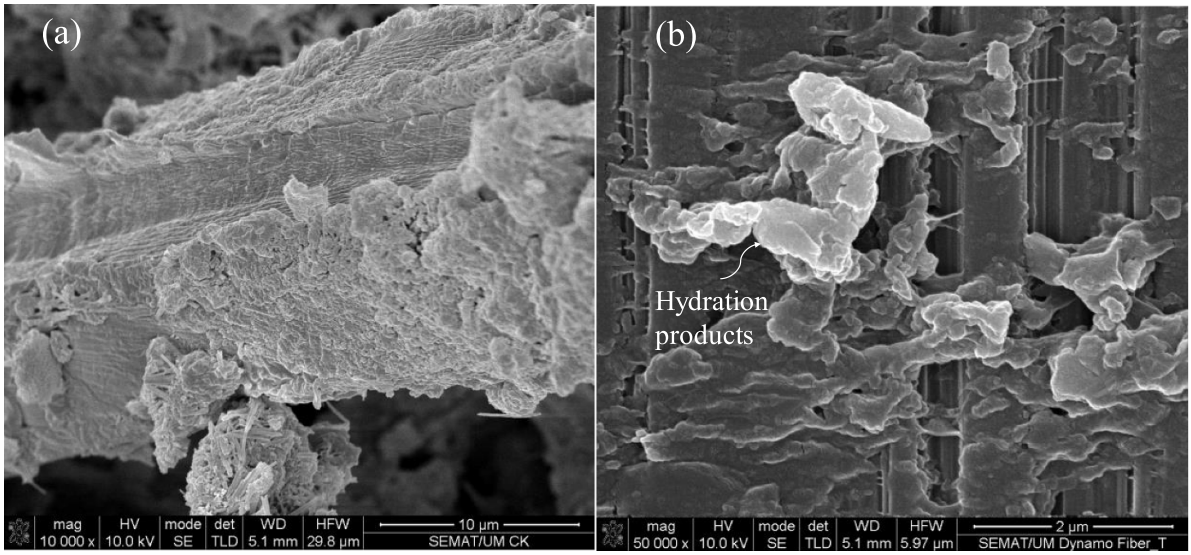

Figure 21. Dyneema fiber surface morphology: (a) low magnification, (b) high magnification.

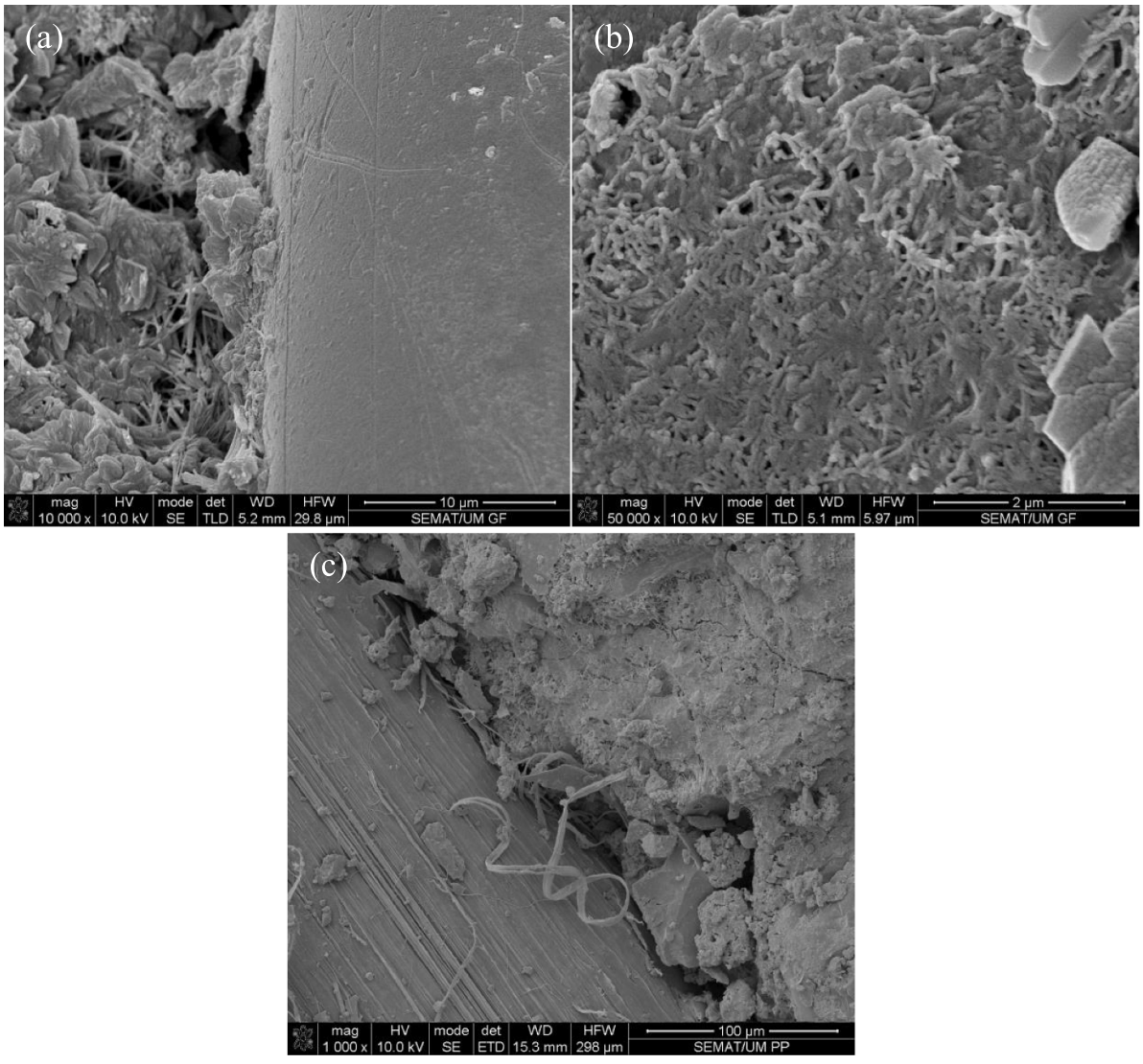

Figure 22. Glass and PP fiber surface morphology: (a) low magnification of glass fiber, (b) high magnification of glass fiber, (c) PP fiber.

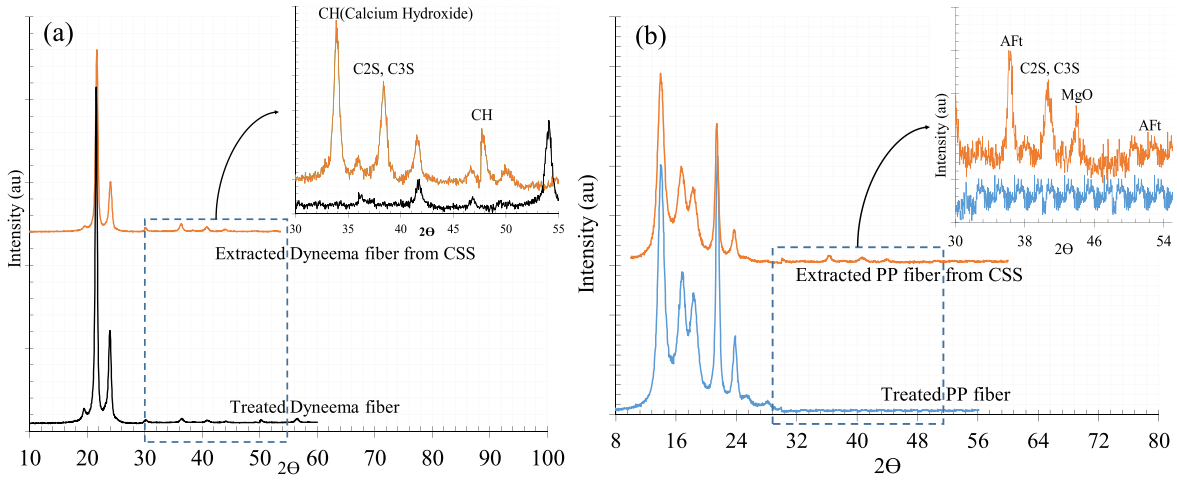

Figure 23. The XRD patterns of treated and extracted fiber from the CS: (a) Dyneema fiber, (b) PP fiber.

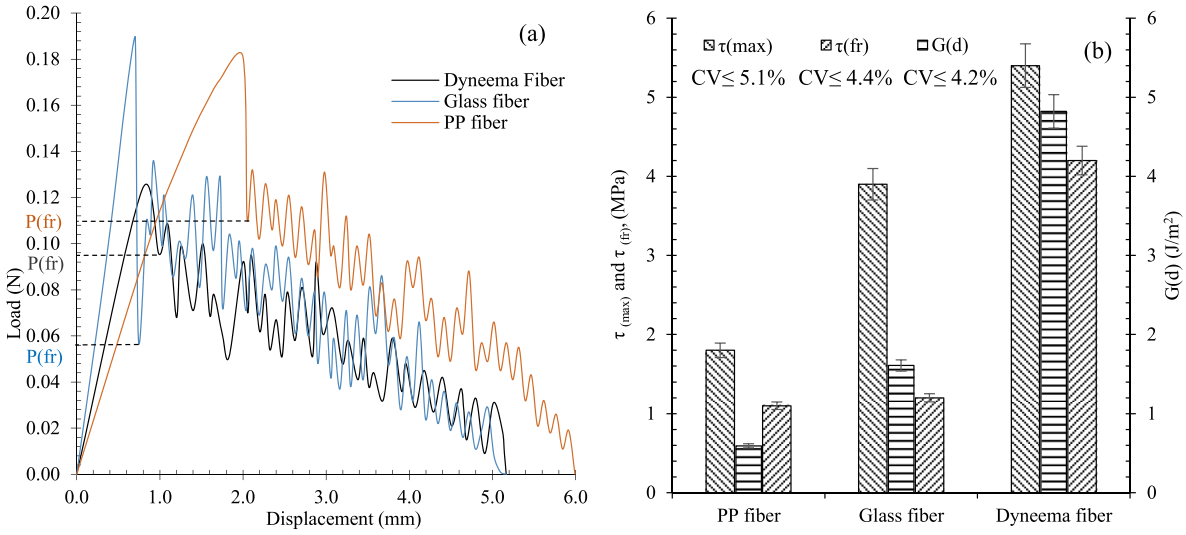

Figure 24. The single-fiber pullout test results of different fibers: (a) pull-out load/displacement curves and (b) interfacial properties.

shown in figure 24(b). As can be apperceived the chemical debonding energy (G_d) and frictional bond strength (τ_{fr}) of the PP fiber are about 0.59 J m^{-2} and 1.1 MPa respectively, and the bond strength (τ_{max}) for this fiber was obtained around 1.8 MPa. This result shows that frictional bond strength acts a crucial role in the PP bond strength among the cementitious matrix.

As can be apperceived the chemical debonding energy (G_d) and frictional bond strength (τ_{fr}) of the PP fiber are about 0.59 J m^{-2} and 1.1 MPa respectively, and the bond strength (τ_{max}) for this fiber was obtained around 1.8 MPa. This result shows that frictional bond strength acts a crucial role in the PP bond strength among the cementitious matrix. In the case of glass fibers, (G_d), (τ_{fr}), and (τ_{max}) were obtained around 1.6 J m^{-2}, 1.2, and 3.9 MPa, respectively, which indicate the efficiency of chemical bonding in terms of interfacial performance improvement. Besides these results showed 2.7, 1.1, and 2.16 times increment respectively relative to the PP fibers. The amount of interfacial properties in the case of Dyneema fiber were even further improved so that the (G_d), (τ_{fr}), and (τ_{max}) were achieved around 3, 3.5, and 1.3 times more compared to the Glass fiber, i.e. around 4.8 J m^{-2}, 4.2, and 5.4 MPa respectively.

3.3. Mechanical properties

The UCS of reinforced CS with different types and concentration of fibers after 28 d of hydration is shown in figure 25. As can be observed the incorporation of certain concentrations of the fibers into the CS caused an increase in the UCS of the composite where this concentration was heavily dependent on the properties of the fibers. Indeed, reinforcing CS containing 0.17% of CNMs by 0.5% PP fibers, increased the UCS

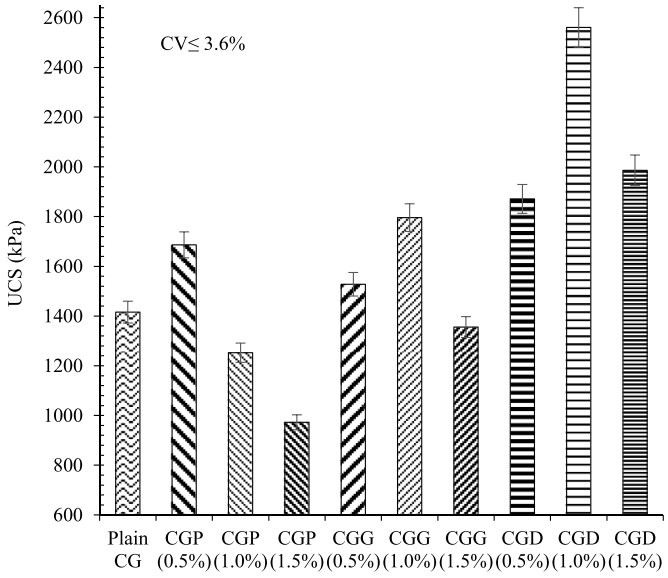

Figure 25. Unconfined compressive strength (UCS) of reinforced CS with different types and concentrations of the fibers after 28 d of hydration.

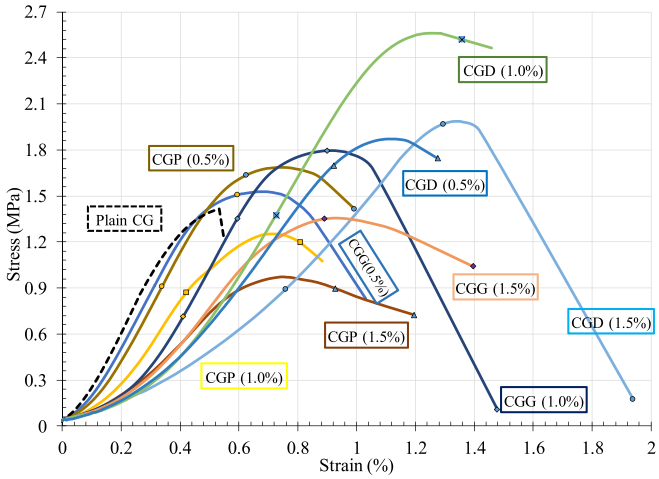

Figure 26. The stress–strain curves of reinforced CS with different types and concentration of the fibers after 28 d of hydration.

by around 21% compared to the plain specimen while excessive increasing of the PP fibers concentration to 1.0%, and 1.5%, led to the reduction of the CS of around 11% and 31%, respectively.

In the case of glass fibers, the incorporation of 0.5% and 1.0% glass fiber into the composite increased the UCS by about 8% and 29%, respectively, and increasing the fiber concentration beyond 1.0%–1.5% caused a UCS reduction of around 6%. The trend of the results in Dyneema fibers showed a different narrative, reinforcing the CS by all concentration of Dyneema fibers in the range of 0.5%–1.5% led to the improvement of the UCS in such a way that incorporation of 0.5%, 1.0%, and 1.5% caused the UCS increment by around 32%, 82%, and 40% compared to the plain CS.

Hence, based on the above results, the optimum concentration of the PP was obtained around 0.5% in terms of the UCS enhancement, while this amount for glass and Dyneema fibers was approximately 1.0%.

The reason for this issue is dependent on the surface condition, aspect ratio, and ductility of the fibers. Indeed, a certain ratio of the ductility and strength of fiber is required to avoid the occurrence of the shear rupture on the surface and/or around the fiber particularly in the case of high interaction between the fiber and composite.

The stress–strain curves of reinforced CS with different types and concentration of the fibers after 28 d of hydration, are shown in figure 26.

The results showed that incorporation of fibers into the CS increased the ductility of the composite. A similar trend was reported in other studies performed on the effects of PP and glass fibers on the mechanical behavior of cementitious stabilized sand [31, 78–80]. As illustrated in figure 26, specimens composed of Dyneema fibers showed more ductile behavior and also more dissipated energy after failure.

The axial strain at failure (maximum stress) and the tangent modulus at 50% of the peak stress ($E_{(50\%)}$) of reinforced CS with different types and concentrations of the fibers, which is shown in figure 27, also proved this issue. Indeed, as can be seen, the incorporation of 0.5%, 1.0%, and 1.5% PP fibers into the CS containing 0.17% of CNMs, increased the failure strain by around 30%, 38%, and 44%, while this amounts for glass fiber reinforcement, were obtained 26%, 67%, and 75% respectively. The failure strain increment of CS affected by Dyneema fiber reinforcement were 106%, 142%, and 153%, respectively.

The addition of fiber also decreased the $E_{(50\%)}$ of the CS such a way that the incorporation 0.5%, 1.0%, and 1.5% PP fiber into the composite reduced the $E_{(50\%)}$ by around 12%, 27%, and 50% in comparison to the plain CS. Reinforcing of the CS by similar concentration of glass fibers also caused a reduction in the $E_{(50\%)}$ by 10%, 17%, and 40%, respectively, while these amounts for Dyneema fibers were around 35, 25, and 46%.

3.4. Durability evaluations

In order to evaluate the durability of fiber-reinforced CS, we calculated the weight loss of the composite during 12 cycles of wetting and drying, and this is presented in figure 28.

The results showed that the incorporation of PP fibers in the range of 0.5%–1.5% into the CS composite led to the reduction of composite resistance against wetting and drying cycles in such a way that specimens composed of 0.5%, 1.0%, and 1.5% PP lost weight of around 2.63%, 3.17%, and 3.9%, respectively.

Reinforcing plain CS containing 0.17% CNMs with glass and Dyneema fibers increased the composite durability; however, excessive increases of the fiber concentration beyond 1.0% caused an increase in the weight loss against wetting and drying cycles that showed a downward trend in terms of durability.

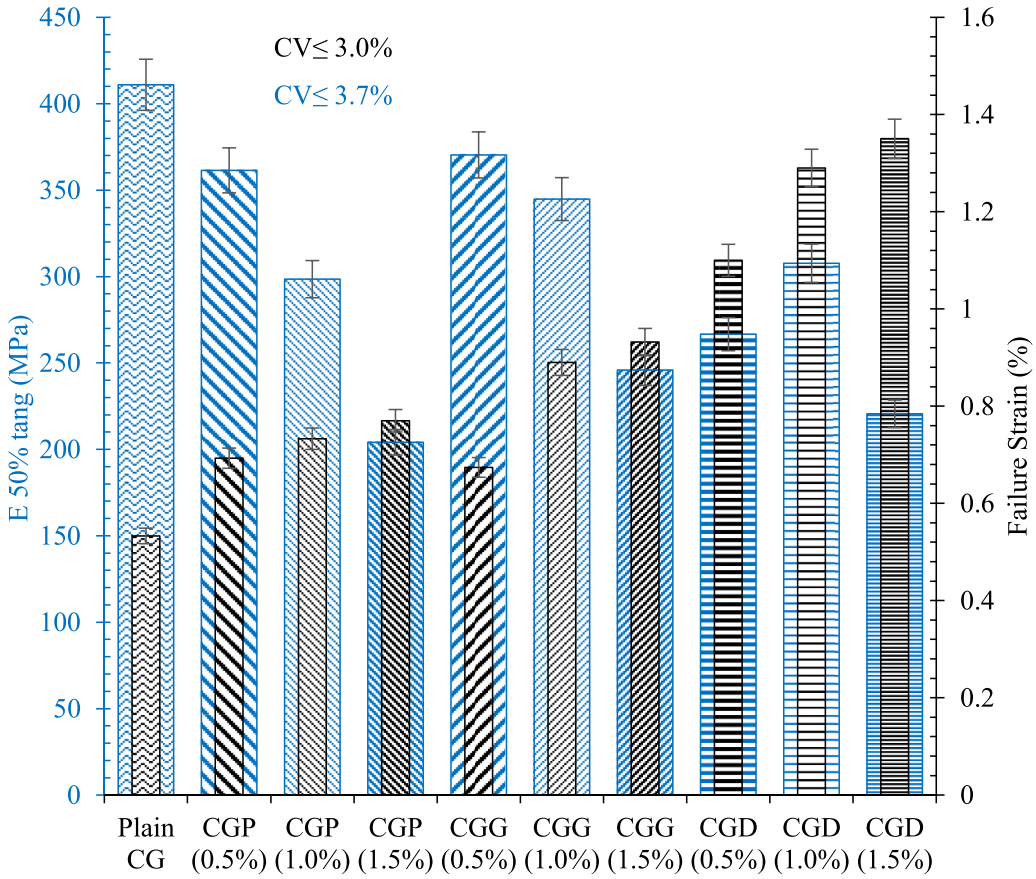

Figure 27. The amounts of the strain at rupture point and $E_{(50\%)}$ for reinforced CS with different types and concentrations of the fibers after 28 d of hydration.

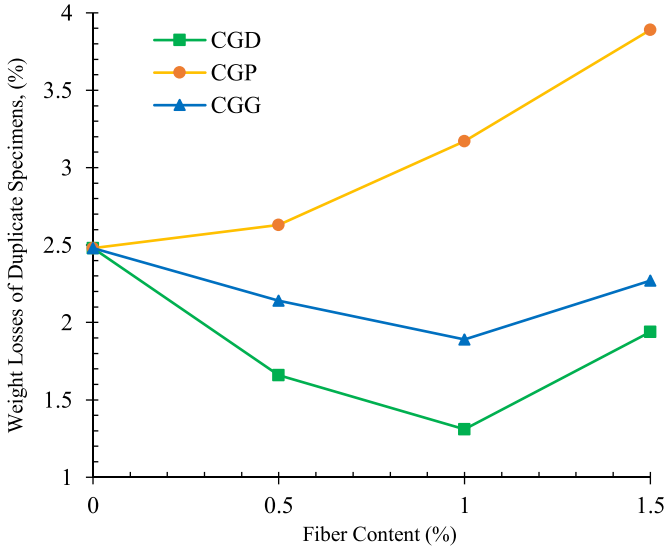

Figure 28. Weight loss of reinforced CS with different types and concentrations of the fibers against wetting and drying cycles.

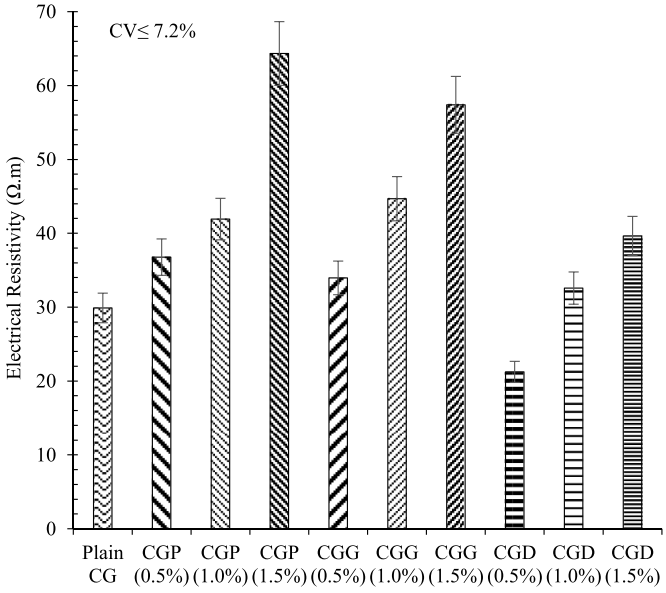

Figure 29. Electrical resistivity of reinforced CS with different types and concentrations of fibers after 72 h of oven-drying.

The incorporation 0.5%, 1.0%, and 1.5% glass and Dyneema fiber into the plain CS demonstrated 2.1%, 1.8%, and 2.2% as well as 1.6%, 1.3%, and 1.9% weight loss, respectively, while this amount for plain CS was obtained at around 2.5%.

3.5. Piezoresistivity investigations

3.5.1. Electrical resistivity. The results of the electrical resistivity measurements for reinforced CS with different types

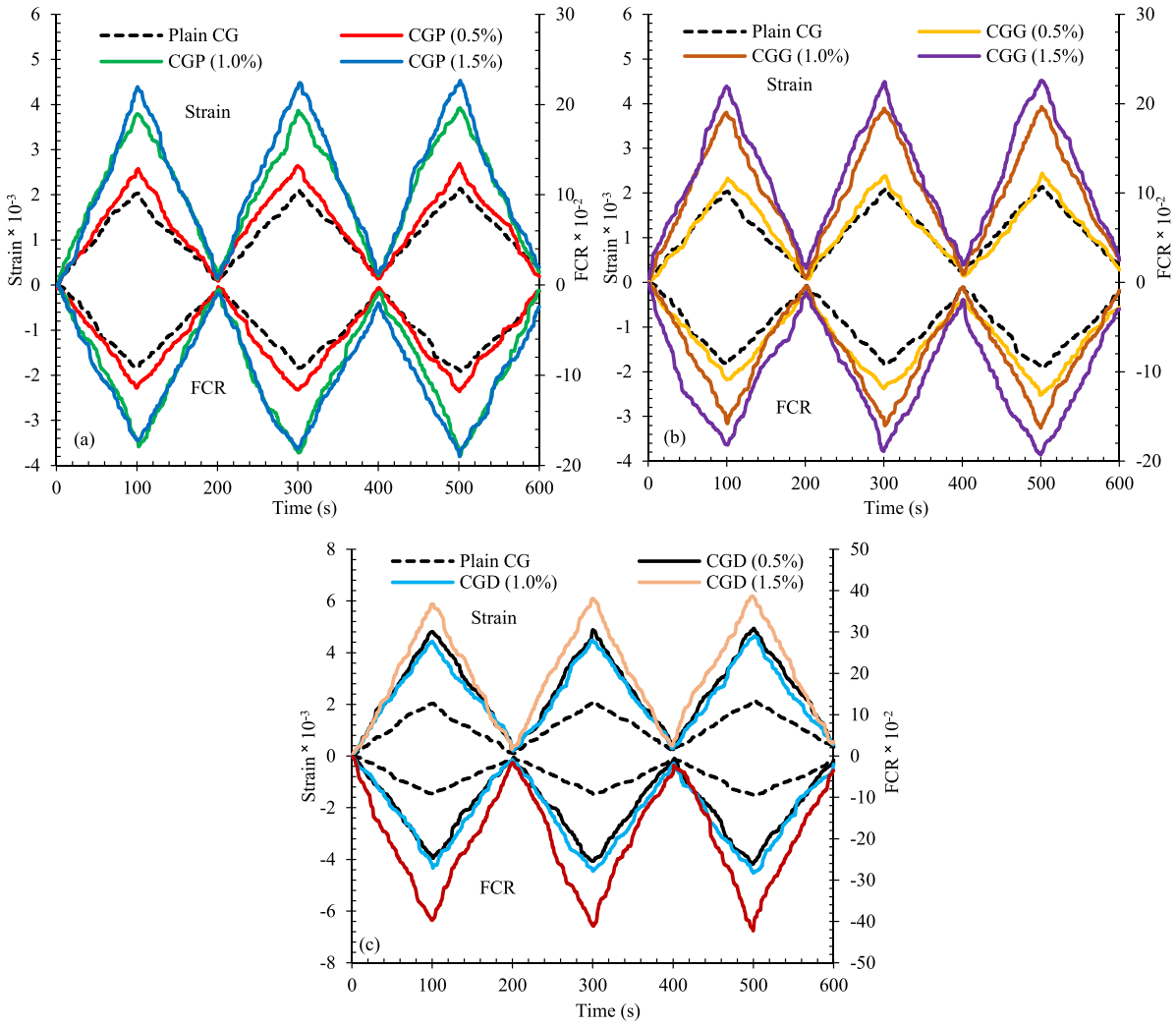

Figure 30. Variation of the fractional changes in the electrical resistivity (FCR) vs. the strain for reinforced CS with different types and concentrations of the fibers: (a) PP fiber, (b) glass fiber, (c) Dyneema fiber.

and concentrations of the fibers after 72 h of oven-drying are shown in figure 29. It is clear that incorporation of microfiber into the plain CS, which contained 0.17% hybrid CNT/GNP, reduced the electrical conductivity of the composite.

As can be observed reinforcing the CS by 0.5%, 1.0%, and 1.5% PP and glass fibers caused a reduction in the electrical conductivity by around 23%, 40%, and 115% as well as 13%, 49%, and 92%, respectively. This indicates that the reinforcing of the composite by microfibers is likely to increase the percolation threshold. Besides the rectangular shape of the PP cross-section with relatively large dimensions increased the electrical resistivity of the composite more than with glass fibers. The non-conductive microfiber with a dense microstructure also acted as a large obstacle and reduced the electron tunneling effects.

In the case of Dyneema fiber, a different trend was observed. Although, the addition of the low fiber concentration to the CS increased the conductivity of the composite, increasing the fiber concentration reduced this. The specimen composed of (0.5) % of Dyneema fiber showed a resistivity reduction of around 29%, while the electrical resistivity of the specimens containing 1.0% and 1.5% Dyneema demonstrated 10% and 32% more electrical resistivity than plain CS, respectively. The smaller cross-section and porous structure of the Dyneema fiber which can absorb a negligible amount of water is likely the reason for this issue.

3.5.2. Piezoresistivity response under cyclic compression test. The variation of fractional changes in the electrical resistivity and axial strain under cyclic compression loading for different fiber-reinforced composites is illustrated in figure 30. Generally, under compression cyclic loading, the negative values were achieved for FCR due to the decrease in electrical resistance during loading compared to the primary electrical resistance (equation (7)). In compression loading, the conductive path becomes closer together, which causes an increase in the electrical conductivity and, consequently, reduces the electrical resistivity. The results showed that the changes in electrical resistivity increased by increasing the strain affected by the load increasing, and, in contrast, the FCR was decreased by load reduction.

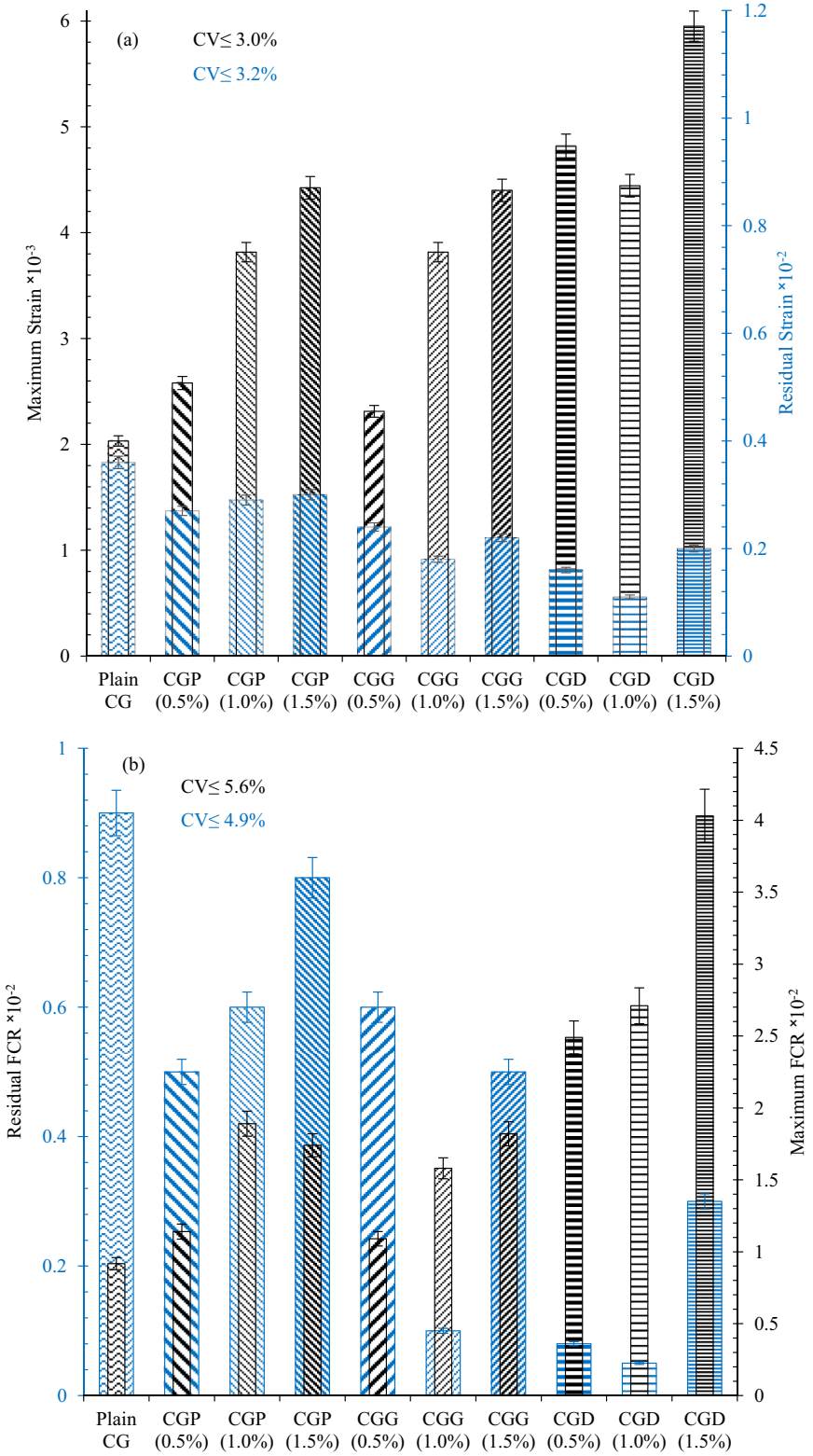

Figure 31. The strain and FCR for fiber-reinforced and non-reinforced specimens: (a) maximum and residual strain, (b) maximum and residual FCR.

At the end of each loading cycle, a lower residual strain and FCR remained in the fiber-reinforced specimen compared to the plain CS, which contained 0.17% CNM. This is likely due to the ductility improvement of the fiber-reinforced composite. The maximum amount of strain and the FCR in addition to the residual strain and FCR at the end of the third cycle of the loading for fiber-reinforced and non-reinforced specimens are shown in figure 31. The results showed that the maximum

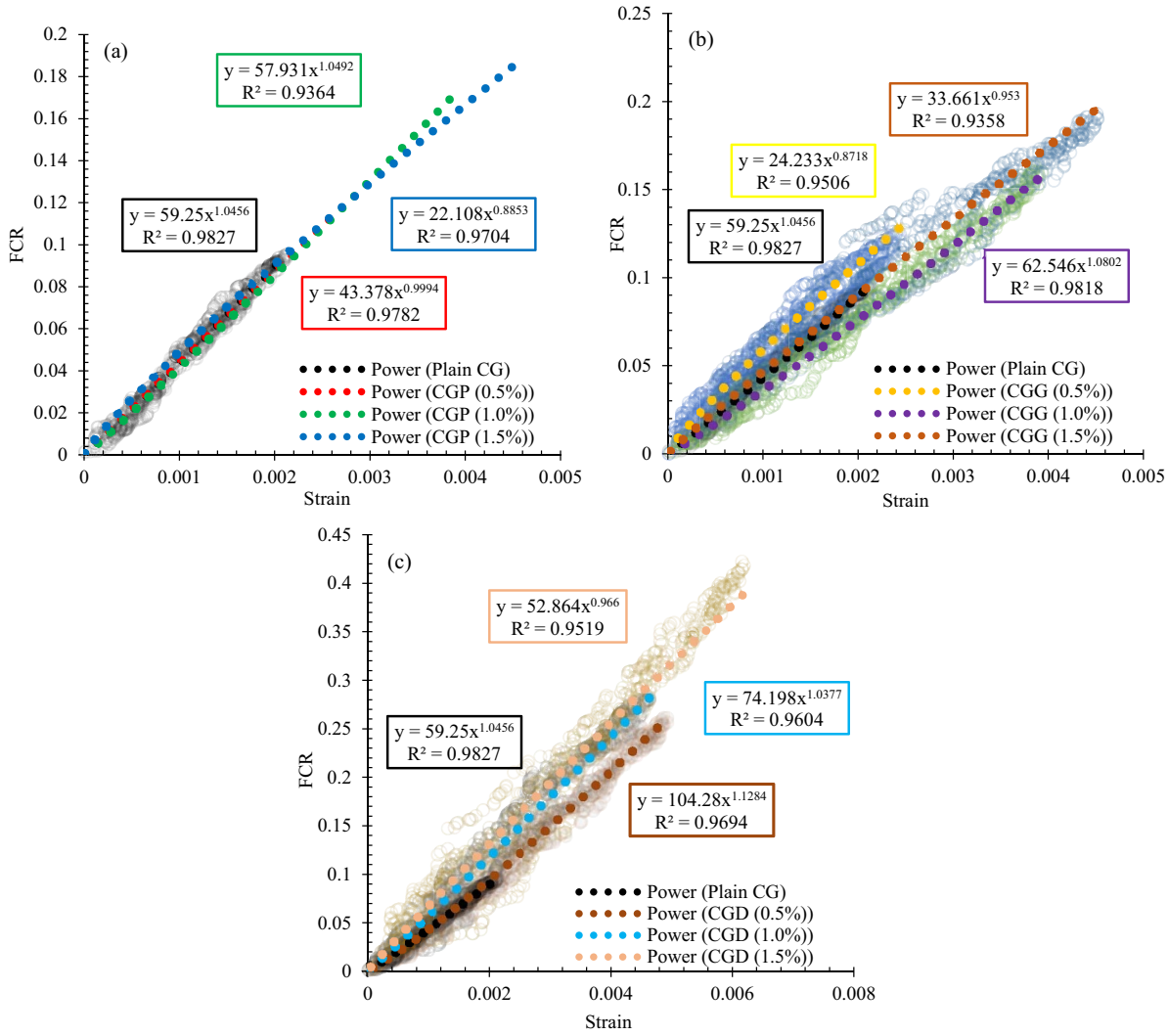

Figure 32. The relation between the FCR and strain for reinforced CS with different types and concentrations of fibers: (a) PP fiber, (b) glass fiber, (c) Dyneema fiber.

amounts of strain and FCR for fiber-reinforced specimens at the pick of the load were higher than plain composite. However, the residual strain and FCR at the end of unloading were much lower, which indicates the positive effects of fiber in terms of ductility behavior enhancement and, consequently, the more stable and reliable piezoresistivity behaviors.

What's more, the incorporation of the fiber into the CS can prevent crack propagation due to a reduction of the stiffness, which can improve the long-term performance. By comparing the results of this study with previous research [10], we also found that the residual strain and FCR in the fiber-reinforced specimen were significantly lower than the composite, which was only composed of CNT and GNPs.

The results also showed an increase in the FCR and strain at the end of loading that becomes increase by increasing the loading cycle number. These amounts were more obvious in the PP and glass fiber-reinforced specimens, particularly with high fiber concentrations. As can be observed in figures 30(a) and (b), in PP and glass fiber-reinforced composites, the amounts of the FCR increased with the increasing fiber concentration due to the increasing strain and ductility of the specimens.

In the case of Dyneema fiber-reinforced CS (figure 30(c)), increasing the fiber concentration from 0.5% to 1.0% reduced the FCR, due to the strain reduction affected by the higher stiffness of this specimen, while by increasing the fiber concentration to (1.5)%, the strain and consequently FCR was increased again.

In order to better evaluate the relation between fractional changes in the electrical resistivity and strain under cyclic compressive loading, the variation of FCR together with the axial strain for different fiber-reinforced specimens is presented in figure 32. Generally, the power functions were found to better express the relation between the FCR and strain.

In PP fiber-reinforced CS (figure 32(a)), however, the slopes of the curves were increased sharply at the initial phase of the loading, the slope was decreased by excessive load increasing, which indicates an excessive reduction of the distance between the conductive paths due to high strain, which prevents significant changes.

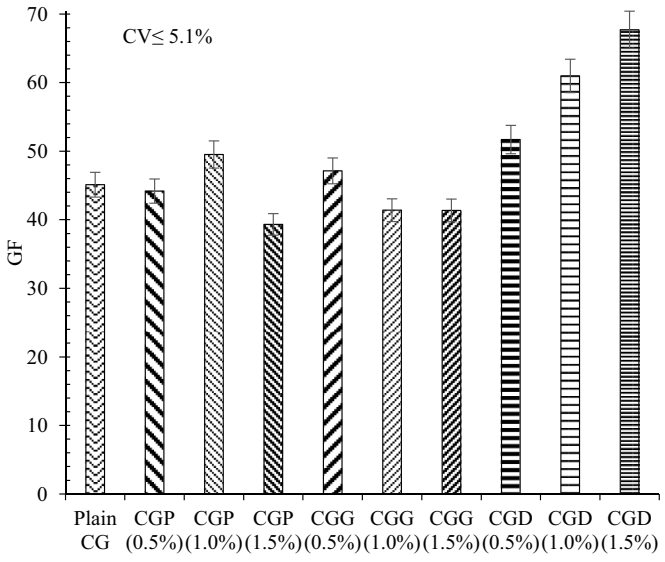

Figure 33. Gauge factor variations for reinforced CS with different types and concentrations of the fibers: (a) PP fiber, (b) glass fiber, (c) Dyneema fiber.

This ambivalent trend was more explicit in specimen CGP (1.5)%, which contained a higher amount of PP fiber and showed more ductile behavior. It should be noted that the scatters of the data were also decreased by increasing the PP fiber concentration. In the case of glass fiber-reinforced CS (figure 32(b)), this ambivalent trend was observed in the slopes of the curves, especially in specimen CGG (1.5)%. In the glass fiber-reinforced composites, the scatter of the data was also reduced by increasing the fiber concentration.

In the Dyneema reinforced specimens (figure 32(c)), a reverse trend was observed, and the scattering of the data was increased by increasing the fiber concentration due to the mechanical interactions between the composite components and fibers under the load. In Dyneema reinforced specimens, however, the slopes of the curves were gradually raised by the increasing fiber concentration, the ambivalent trend was still visible in the curve slopes.

3.5.3. Gauge factors. The results of calculated gauge factors for reinforced CS with different types and concentration of the fibers are demonstrated in figure 33.

The amounts of the strain and FCR are two effective parameters in terms of determining the sensitivity or the gauge factor of the specimen (equation (8)). By considering this issue and the above discussions, as can be observed in figure 33, the maximum gauge factors were achieved for Dyneema fiber-reinforced specimens in such a way that specimens composed of 0.5%, 1.0%, and 1.5% of Dyneema fibers showed gauge factors equivalent to 52, 61, and 68, respectively, while the gauge factor of the plain CS containing 0.17% CNMs was about 45.

In the case of PP and glass fiber-reinforced composite, the incorporation of 0.5%, 1.0%, and 1.5% fibers into the CS, led to a gain in the gauge factors equal to 44, 49, 39, and 47, 42, 41 respectively.

4. Sustainable issues

Sustainability focuses on addressing the desires of the present without undermining the ability of future generations to fulfill their requirements. The concept of sustainability is composed of three pillars: environmental friendliness, economics, and social values also known informally as the planet, profits, and people [81].

Generally, the AR-glass fiber has lower environmental impacts compared with polymer-based fibers, such as PP and Dyneema [82, 83]. Given that the approximate price of AR-glass fiber and propylene is the same and is about one-third of the Dyneema fibers, this makes the AR-glass fibers appear more ideal, despite the high impact of Dyneema compared to glass fibers. Indeed, in a project where high sensitivity, ductility, and strength of the composite is not required, the remarkable effects of Dyneema fiber in terms of 82% UCS improvement, 25% elastic modulus reduction, and a gauge factor equal to 61, can be balanced with a low cost solution satisfied by glass fiber with 29% UCS improvement, 17% modulus reduction, and a gauge factor equal to 42.

5. Conclusions

In this study, the effects of the fibers on the physical, mechanical, durability, microstructure, and piezoresistivity behavior of reinforced cemented sand (CS) incorporating hybrid CNT and GNP were evaluated to achieve a novel ductile self-sensing fiber-reinforced cementitious composite. For this purpose, 0.5%, 1.0%, and 1.5% of a novel fiber called Dyneema and two conventional fibers, glass and polypropylene, were treated by chemical methods and incorporated into the CS containing 0.17% hybrid CNT/GNP (1:1). From the experimental results obtained and deeply analyzed after 28 d of hydration in at least 144 of the compacted composites, our conclusions are summarized as follows:

- SEM, EDX, XRD, and FTIR analysis of the fibers showed that the surface treatments of PP and Dyneema fibers with sulfuric acid, in addition to surface roughing and rippling, caused the formation of different oxygen functional groups on the fiber surface including: (–OH), ($–COO^-$), (–O–), and ($–C–SO_3^-$). Treatment of the glass fiber with hydrofluoric acid also led to the formation of (–OH), (–SiF), and (–ZnF) functional groups on its surface.
- The single fiber pullout test also showed great interfacial performance for Dyneema fiber so that chemical debonding energy, frictional bond strength, and bond strength of this fiber were obtained 3, 3.5, and 1.3 times more than Glass and 8.1, 3.8, and 3 times more than PP fiber respectively.
- The incorporation of PP fiber with concentrations in the range of 0.5%–1.5%, into the plain CS, which contained 0.17% CNMs, reduced the UCS. Although increasing the glass and Dyneema fiber up to 1.0% increased the UCS of the CS (29% and 82% respectively). An excessive increasing of the fiber concentration led to a UCS reduction.

- Evaluation of the tangent modulus at 50% of the peak stress ($E_{(50\%)}$) for the fiber-reinforced specimens demonstrated that Dyneema, glass, and PP fibers were respectively more efficient in terms of ductility improvement of the composite.
- Reinforcing the plain CS with 0.5%, 1.5%, and 1.5% of PP fiber led to increasing the optimum water content as well as a reduction in the maximum dry density. While the incorporation 1.0% of the glass and Dyneema fiber increased the maximum dry density and caused a reduction in the optimum water content. It should be noted that increasing the fiber concentration beyond 1.0% reduced the maximum dry density and increased the optimum water content. A quasi unique relation between $\gamma_d/\gamma_{d\max}$ vs. "Sr–Sr (opt)" showed the potential for real field applications.
- The non-destructive ultrasonic test also showed a denser microstructure after 28 d of hydration for reinforced CS by 1.0% of Dyneema and glass fibers compared to the other specimens.
- The Dyneema and glass fibers showed better bonding and interactions with the cementitious matrix.
- Specimens reinforced by 1.0% of Dyneema and glass fibers demonstrated a lower weight loss after 12 wetting and drying cycles (durability) compared to the other specimens.
- The maximum gauge factors were achieved for Dyneema fiber-reinforced specimens in such a way that specimens composed of 0.5%, 1.0%, and 1.5% Dyneema fibers showed gauge factors equivalent to 52, 61, and 68 respectively, while the gauge factor of the plain CS containing 0.17% CNMs obtained about 45. In the case of PP and glass fiber-reinforced composites, the incorporation of 0.5%, 1.0%, and 1.5% fibers into the CS, led to a gain in the gauge factors equal to 44, 49, and 39, as well as 47, 42, and 41, respectively.
- From a sustainable perspective, the reinforcement with glass fiber could be a compromise to achieve a low cost and environmentally friendly solution for the development of a novel self-sensing fiber-reinforced cementitious composite.

In summary, we believe that this novel approach contributes to the new era of smart composite materials in intelligent structures. However, the high stiffness and low ductility of the CNMs reinforced composite makes them prone to cracking which necessitates further research in order to achieve solutions to increase their ductility such as fiber reinforcements.

Data availability statement

The data that support the findings of this study are available upon reasonable request from the authors.

Acknowledgments

This work was supported by the European Commission-Shiff2Rail Program under the project 'IN2TRACK2–826255-H2020-S2RJU-2018/H2020-S2RJU CFM-2018'. It is also partly financed by FCT/MCTES through national funds (PIDDAC) under the R&D Unit Institute for Sustainability and Innovation in Engineering Structures (ISISE), under reference UIDB/04029/2020, as well as under the R&D Unit Centre for Textile Science and Technology (2C2T).

Conflicts of interest

The authors declare no conflict of interest for this research work.

Author contributions

M A, R F and A G C: conceptualization, methodology, validation, formal analysis, investigation, resources, data curation, writing original draft preparation, writing review and editing, visualization; A G C and R F: supervision, project administration, funding acquisition. All authors have read and agreed to the published version of the manuscript.

ORCID iDs

Mohammadmahdi Abedi https://orcid.org/0000-0002-2920-9284
Raul Fangueiro https://orcid.org/0000-0003-3303-6563
António Gomes Correia https://orcid.org/0000-0002-0103-2579

References

[1] Wang C S, Wu F and Chang F-K 2001 Structural health monitoring from fiber-reinforced composites to steel-reinforced concrete *Smart Mater. Struct.* **10** 548–52
[2] Han B, Yu X and Kwon E 2009 A self-sensing carbon nanotube/cement composite for traffic monitoring *Nanotechnology* **20** 445501
[3] Suchorzewski J, Prieto M and Mueller U 2020 An experimental study of self-sensing concrete enhanced with multi-wall carbon nanotubes in wedge splitting test and DIC *Constr. Build. Mater.* **262** 120871
[4] Yoo D-Y, You I, Zi G and Lee S-J 2019 Effects of carbon nanomaterial type and amount on self-sensing capacity of cement paste *Measurement* **134** 750–61
[5] Yoo D-Y, You I and Lee S-J 2018 Electrical and piezoresistive sensing capacities of cement paste with multi-walled carbon nanotubes *Arch. Civ. Mech. Eng.* **18** 371–84
[6] Dong W, Li W, Shen L, Sun Z and Sheng D 2020 Piezoresistivity of smart carbon nanotubes (CNTs) reinforced cementitious composite under integrated cyclic compression and impact *Compos. Struct.* **241** 112106
[7] Wen S and Chung D D L 2001 Uniaxial compression in carbon fiber-reinforced cement, sensed by electrical resistivity measurement in longitudinal and transverse directions *Cement Concr. Res.* **31** 297–301
[8] Azhari F and Banthia N 2012 Cement-based sensors with carbon fibers and carbon nanotubes for piezoresistive sensing *Cem. Concr. Compos.* **34** 866–73
[9] You I, Yoo D-Y, Kim S, Kim M-J and Zi G 2017 Electrical and self-sensing properties of ultra-high-performance fiber-reinforced concrete with carbon nanotubes *Sensors* **17** 2481
[10] Abedi M, Fangueiro R and Correia A G 2020 Ultra-sensitive affordable cementitious composite with high mechanical and microstructural performances by hybrid CNT/GNP *Materials* **13** 3484

[11] García-Macías E, D'Alessandro A, Castro-Triguero R, Pérez-Mira D and Ubertini F 2017 Micromechanics modeling of the uniaxial strain-sensing property of carbon nanotube cement-matrix composites for SHM applications *Compos. Struct.* **163** 195–215
[12] Choi Y C 2021 Cyclic heating and mechanical properties of CNT reinforced cement composite *Compos. Struct.* **256** 113104
[13] Ding S, Ruan Y, Yu X, Han B and Ni Y Q 2019 Self-monitoring of smart concrete column incorporating CNT/NCB composite fillers modified cementitious sensors *Constr. Build. Mater.* **201** 127–37
[14] Kim H K, Nam I W and Lee H K 2014 Enhanced effect of carbon nanotube on mechanical and electrical properties of cement composites by incorporation of silica fume *Compos. Struct.* **107** 60–9
[15] Kim G M, Nam I W, Yang B, Yoon H N, Lee H K and Park S 2019 Carbon nanotube (CNT) incorporated cementitious composites for functional construction materials: the state of the art *Compos. Struct.* **227** 111244
[16] Goldfeld Y, Quadflieg T and Gries T 2017 Sensing capabilities of carbon based TRC beam from slack to pull-out mechanism *Compos. Struct.* **181** 294–305
[17] Ferreira A D B L, Nóvoa P R O and Marques A T 2016 Multifunctional material systems: a state-of-the-art review *Compos. Struct.* **151** 3–35
[18] Han B, Ding S and Yu X 2015 Intrinsic self-sensing concrete and structures: a review *Measurement* **59** 110–28
[19] Dong W, Li W, Tao Z and Wang K 2019 Piezoresistive properties of cement-based sensors: review and perspective *Constr. Build. Mater.* **203** 146–63
[20] Han B G, Han B Z and Ou J P 2009 Experimental study on use of nickel powder-filled Portland cement-based composite for fabrication of piezoresistive sensors with high sensitivity *Sens. Actuators* A **149** 51–5
[21] Yoo D-Y, You I, Youn H and Lee S-J 2018 Electrical and piezoresistive properties of cement composites with carbon nanomaterials *J. Compos. Mater.* **52** 3325–40
[22] Tao J, Wang J and Zeng Q 2020 A comparative study on the influences of CNT and GNP on the piezoresistivity of cement composites *Mater. Lett.* **259** 126858
[23] Gupta T K, Choosri M, Varadarajan K M and Kumar S 2018 Self-sensing and mechanical performance of CNT/GNP/UHMWPE biocompatible nanocomposites *J. Mater. Sci.* **53** 7939–52
[24] Abedi M, Fangueiro R and Correia A G 2020 An effective method for hybrid CNT/GNP dispersion and its effects on the mechanical, microstructural, thermal, and electrical properties of multifunctional cementitious composites *J. Nanomater.* **2020** 6749150
[25] Luan C, Yao X, Zhang C, Wang B and Fu J 2019 Large-scale deformation and damage detection of 3D printed continuous carbon fiber reinforced polymer-matrix composite structures *Compos. Struct.* **212** 552–60
[26] Alrekabi S, Cundy A B, Lampropoulos A, Whitby R L D and Savina I 2017 Mechanical performance of novel cement-based composites prepared with nano-fibres, and hybrid nano- and micro-fibres *Compos. Struct.* **178** 145–56
[27] Liew K M, Kai M F and Zhang L W 2017 Mechanical and damping properties of CNT-reinforced cementitious composites *Compos. Struct.* **160** 81–8
[28] Lee S-J, Jeong S-H, Kim D-U and Won J-P 2020 Effects of graphene oxide on pore structure and mechanical properties of cementitious composites *Compos. Struct.* **234** 111709
[29] Lushnikova A and Zaoui A 2018 Influence of single-walled carbon nantotubes structure and density on the ductility of cement paste *Constr. Build. Mater.* **172** 86–97
[30] Abedi M, Fangueiro R and Correia A G 2021 Development of a novel multifunctional cementitious-based geocomposite by the contribution of CNT and GNP *Nanomaterials* **11** 961
[31] Khajeh A, Jamshidi Chenari R and Payan M 2020 A simple review of cemented non-conventional materials: soil composites *Geotech. Geol. Eng.* **38** 1019–40
[32] Yoo D-Y, Kim S, Park G-J, Park J-J and Kim S-W 2017 Effects of fiber shape, aspect ratio, and volume fraction on flexural behavior of ultra-high-performance fiber-reinforced cement composites *Compos. Struct.* **174** 375–88
[33] Wu F, Xu L, Chi Y, Zeng Y, Deng F and Chen Q 2020 Compressive and flexural properties of ultra-high performance fiber-reinforced cementitious composite: the effect of coarse aggregate *Compos. Struct.* **236** 111810
[34] Esfandiari J and Soleimani E 2018 Laboratory investigation on the buckling restrained braces with an optimal percentage of microstructure, polypropylene and hybrid fibers under cyclic loads *Compos. Struct.* **203** 585–98
[35] Consoli N C, Montardo J P, Donato M and Prietto P D 2004 Effect of material properties on the behaviour of sand—cement—fibre composites *Proc. Inst. Civ. Eng.* **8** 77–90
[36] Daniels J L and Inyang H I 2004 Contaminant barrier material textural response to interaction with aqueous polymers *J. Mater. Civ. Eng.* **16** 265–75
[37] Kutanaei S S and Choobbasti A J 2016 Triaxial behavior of fiber-reinforced cemented sand *J. Adhes. Sci. Technol.* **30** 579–93
[38] Anagnostopoulos C A, Tzetzis D and Berketis K 2014 Shear strength behaviour of polypropylene fibre reinforced cohesive soils *Geomech. Geoeng.* **9** 241–51
[39] Consoli N C, Moraes R and Festugato L 2013 Variables controlling strength of fibre-reinforced cemented soils *Proc. Institution of Civil Engineers–Ground Improvement* **166** 221–32
[40] Festugato L, Menger E, Benezra F, Kipper E A and Consoli N C 2017 Fibre-reinforced cemented soils compressive and tensile strength assessment as a function of filament length *Geotext. Geomembr.* **45** 77–82
[41] Goeman F 1980 Inhibitors for alkali-glass reactions in glass fiber reinforced cement products *Composites* **11** 56
[42] (Available at: https://fibrxl.com/fibrxl-performance/fibers/dyneema/) (Accessed October 2020)
[43] Abedi M, Fangueiro R, Camões A and Gomes Correia A 2020 Evaluation of CNT/GNP's synergic effects on the mechanical, microstructural, and durability properties of a cementitious composite by the novel dispersion method *Constr. Build. Mater.* **260** 120486
[44] Correia A G, Valente T, Tinoco J, Falcão J, Barata J, Cebola D and Coelho S 2009 Evaluation of mechanical properties of jet grouting columns using different test methods 17th Int. Conf. Soil Mechanics and Geotechnical Engineering (17th ICSMGE) (*5–8 October*, *Egypt*) pp 2169–71 (IOS Press Alexandria)
[45] Silva J, Azenha M, Correia A G and Ferreira C 2013 Continuous stiffness assessment of cement-stabilised soils from early age *Géotechnique* **63** 1419–32
[46] Tinoco J and Correia A G 2014 Prediction of soil-cement mechanical properties by EC2 modified approach based on early age test results *Int. Conf. on Sustainable Civil Infrastructure* (*July 20–22*, *Yichang, Hubei, China*) pp 25–32
[47] Gomes Correia A and Tinoco J 2017 Advanced tools and techniques to add value to soil stabilization practice *Innovative Infrastruct. Solutions* **2** 26
[48] Parveen S, Rana S, Fangueiro R and Paiva M C 2017 Characterizing dispersion and long term stability of concentrated carbon nanotube aqueous suspensions for

fabricating ductile cementitious composites *Powder Technol.* **307** 1–9
[49] Parveen S, Rana S, Fangueiro R and Paiva M C 2015 Microstructure and mechanical properties of carbon nanotube reinforced cementitious composites developed using a novel dispersion technique *Cement Concr. Res.* **73** 215–27
[50] Wang X, He J, Mosallam A S, Li C and Xin H 2019 The effects of fiber length and volume on material properties and crack resistance of basalt fiber reinforced concrete (BFRC) *Adv. Mater. Sci. Eng.* **2019** 7520549
[51] Correia A A S, Venda Oliveira P J and Custódio D G 2015 Effect of polypropylene fibres on the compressive and tensile strength of a soft soil, artificially stabilised with binders *Geotext. Geomembr.* **43** 97–106
[52] Zhao Y, Ling X, Gong W, Li P, Li G and Wang L 2020 Mechanical properties of fiber-reinforced soil under triaxial compression and parameter determination based on the Duncan-Chang model *Appl. Sci.* **10** 9043
[53] Parveen S, Rana S and Fangueiro R 2013 A review on nanomaterial dispersion, microstructure, and mechanical properties of carbon nanotube and nanofiber reinforced cementitious composites *J. Nanomater.* **2013** 710175
[54] Kang S-T, Seo J-Y and Park S-H 2015 The characteristics of CNT/cement composites with acid-treated MWCNTs *Adv. Mater. Sci. Eng.* **2015** 308725
[55] Yu H, Hermann S, Schulz S E, Gessner T, Dong Z and Li W J 2012 Optimizing sonication parameters for dispersion of single-walled carbon nanotubes *Chem. Phys.* **408** 11–6
[56] Baig Z, Mamat O, Mustapha M, Mumtaz A, Munir K S and Sarfraz M 2018 Investigation of tip sonication effects on structural quality of graphene nanoplatelets (GNPs) for superior solvent dispersion *Ultrason. Sonochem.* **45** 133–49
[57] Peled A, Guttman H and Bentur A 1992 Treatments of polypropylene fibres to optimize their reinforcing efficiency in cement composites *Cem. Concr. Compos.* **14** 277–85
[58] McAlpin J J and Chow W Y 1990 Compositions for preparing cement-adhesive reinforcing fibres *Compos. Manuf.* **1** 265
[59] Proctor B A and Yale B 1980 Glass fibres for cement reinforcement *Philosophical Trans. Royal Society of London. Series A, Mathematical and Physical Sciences* **294** 427–36
[60] Ismojo I, Pratama R, Ramahdita G, Syahrial A Z and Chalid M 2018 Feasibility study of chemical treatments on sorghum fibres for compatibility enhancement in polypropylene composites *Mater. Sci. Forum* **929** 70–7
[61] Mobasher B, Dey V, Bauchmoyer J, Mehere H and Schaef S 2019 Reinforcing efficiency of micro and macro continuous polypropylene fibers in cementitious composites *Appl. Sci.* **9** 2189
[62] Wei X and Ku T 2020 New design chart for geotechnical ground improvement: characterizing cement-stabilized sand *Acta Geotech.* **15** 999–1011
[63] Vinoth G, Moon S-W, Moon J and Ku T 2018 Early strength development in cement-treated sand using low-carbon rapid-hardening cements *Soils Found.* **58** 1200–11
[64] Eskandari-Naddaf H and Ziaei-Nia A 2018 Simultaneous effect of nano and micro silica on corrosion behaviour of reinforcement in concrete containing cement strength grade of C-525 *Procedia Manuf.* **22** 399–405
[65] Katz A and Li V C 1996 A special technique for determining the bond strength of micro-fibres in cement matrix by pullout test *J. Mater. Sci. Lett.* **15** 1821–3
[66] Lu M, Xiao H, Liu M, Li X, Li H and Sun L 2018 Improved interfacial strength of SiO2 coated carbon fiber in cement matrix *Cem. Concr. Compos.* **91** 21–8
[67] Katz A and Li V C 1994 Bond properties of micro-fibers in cementitious matrix *MRS Online Proc. Libr. Arch.* **370** 529
[68] Yilmaz Y and Ozaydin V 2013 Compaction and shear strength characteristics of colemanite ore waste modified active belite cement stabilized high plasticity soils *Eng. Geol.* **155** 45–53
[69] Yilmaz Y 2009 Experimental investigation of the strength properties of sand–clay mixtures reinforced with randomly distributed discrete polypropylene fibers *Geosynth. Int.* **16** 354–63
[70] Lin Z, Kanda T and Li V C 1999 On interface property characterization and performance of fiber reinforced cementitious composites *Concr. sci. eng.* **1** 173–4
[71] Peled A, Zaguri E and Marom G 2008 Bonding characteristics of multifilament polymer yarns and cement matrices *Composites* A **39** 930–9
[72] Tao J, Wang X, Wang Z and Zeng Q 2019 Graphene nanoplatelets as an effective additive to tune the microstructures and piezoresistive properties of cement-based composites *Constr. Build. Mater.* **209** 665–78
[73] Baggott R and Gandhi D 1981 Multiple cracking in aligned polypropylene fibre reinforced cement composites *J. Mater. Sci.* **16** 65–74
[74] Tatsuoka F and Correia A G 2016 Importance of controlling the degree of saturation in soil compaction *Procedia Eng.* **143** 556–65
[75] Yu W, Sisi L, Haiyan Y and Jie L 2020 Progress in the functional modification of graphene/graphene oxide: a review *RSC Adv.* **10** 15328–45
[76] Peled A and Bentur A 2003 Quantitative description of the pull-out behavior of crimped yarns from cement matrix *J. Mater. Civ. Eng.* **15** 537–44
[77] Bentur A and Mindess S 2006 Fibre-cement interactions: stress transfer, bond and pull-out *Fibre Reinforced Cementitious Composites* 2nd edn vol 1 (Boca Raton, FL: CRC Press) pp 31–105
[78] Jiang H, Cai Y and Liu J 2010 Engineering properties of soils reinforced by short discrete polypropylene fiber *J. Mater. Civ. Eng.* **22** 1315–22
[79] Consoli N C, RRd M and Festugato L 2011 Split tensile strength of monofilament polypropylene fiber-reinforced cemented sandy soils *Geosynth. Int.* **18** 57–62
[80] Chandra S, Viladkar M N and Nagrale P P 2008 Mechanistic approach for fiber-reinforced flexible pavements *J. Transp. Eng.* **134** 15–23
[81] Gomes Correia A, Winter M G and Puppala A J 2016 A review of sustainable approaches in transport infrastructure geotechnics *Transp. Geotech.* **7** 21–8
[82] Abdulkareem M, Havukainen J and Horttanainen M 2019 How environmentally sustainable are fibre reinforced alkali-activated concretes? *J. Clean. Prod.* **236** 117601
[83] Joshi S V, Drzal L T, Mohanty A K and Arora S 2004 Are natural fiber composites environmentally superior to glass fiber reinforced composites? *Composites* A **35** 371–6